Monthly Notices
of the
ROYAL ASTRONOMICAL SOCIETY

MNRAS **463,** 2425–2442 (2016) doi:10.1093/mnras/stw2067
Advance Access publication 2016 August 19

Extracting the late-time kinetic Sunyaev–Zel'dovich effect

D. Munshi,* I. T. Iliev, K. L. Dixon and P. Coles
Astronomy Centre, School of Mathematical and Physical Sciences, University of Sussex, Brighton BN1 9QH, UK

Accepted 2016 August 15. Received 2016 August 4; in original form 2015 November 11

ABSTRACT

We propose a novel technique to separate the late-time, post-reionization component of the kinetic Sunyaev–Zeldovich (kSZ) effect from the contribution to it from a (poorly understood and probably patchy) reionization history. The kSZ effect is one of the most promising probe of the *missing baryons* in the Universe. We study the possibility of reconstructing it in three dimensions (3D), using future spectroscopic surveys such as the Euclid survey. By reconstructing a 3D template from galaxy density and peculiar velocity fields from spectroscopic surveys we cross-correlate the estimator against CMB maps. The resulting cross-correlation can help us to map out the kSZ contribution to CMB in 3D as a function of redshift thereby extending previous results which use tomographic reconstruction. This allows the separation of the late-time effect from the contribution owing to reionization. By construction, it avoids contamination from foregrounds, primary CMB, tSZ effect as well as from star-forming galaxies. Due to a high number density of galaxies the signal-to-noise ratio (S/N) for such cross-correlational studies is higher, compared to the studies involving CMB power-spectrum analysis. Using a spherical Bessel–Fourier (sFB) transform we introduce a pair of 3D power spectra: $\mathcal{C}_\ell^{\parallel}(k)$ and $\mathcal{C}_\ell^{\perp}(k)$ that can be used for this purpose. We find that in a future spectroscopic survey with near all-sky coverage and a survey depth of $z \approx 1$, reconstruction of $\mathcal{C}_\ell^{\perp}(k)$ can be achieved in a few radial wave bands $k \approx (0.01\text{–}0.5\,h^{-1}$ Mpc) with a S/N ratio of up to $\mathcal{O}(10)$ for angular harmonics in the range $\ell = (200\text{–}2000)$.

Key words: methods: analytical – methods: numerical – methods: statistical.

1 INTRODUCTION

Only 50 per cent of the baryons consistent with the cosmic microwave background radiation and big bang nucleosynthesis observations have been detected observationally (Fukugita & Peebles 2004, 2006); the validation of the standard cosmological model relies on our ability to detect the missing baryons observationally (Bregmann 2007). Using data from the Canada France Hawaii Lensing Survey[1] and the *Planck* satellite,[2] recent studies, that use cross-correlation of the thermal Sunyaev–Zeldovich (tSZ) effect and weak gravitational lensing, have shown that up to 50 per cent of the baryons may reside outside the virial radius of the haloes (Ma et al. 2014). The cosmological simulations too suggest that majority of the intergalactic medium (IGM) are in the form of warm–hot intergalactic medium (WHIM) within a temperature range $10^5 < \mathrm{T} < 10^7$ K (Cen & Ostriker 1999; Dave et al. 2001; Cen & Ostriker 2006). It is also believed that WHIMs reside in moderately overdense structure such as filaments. However, being collisionally ionized these baryons do not leave any footprints in Lyman-α absorption systems. The emission from WHIMs in either UV photons or X-rays is too weak to be detected given the sensitivity of current instruments. Their detection is also difficult in X-ray given the low level of emission from WHIM. Nevertheless, there has been recent progress on detecting WHIM in UV/X-ray band, via Ly-α, O VI, O VII absorption lines, see e.g. Zappacosta et al. (2004). However, the baryons in the cosmic web have sufficient velocity and column density to produce a detectable cosmic microwave background (CMB) secondary anisotropy effect known as the kinetic Sunyaev–Zel'dovich (kSZ) effect (Sunyaev & Zeldovich 1980).

CMB secondary anisotropies arise at all angular scales; the largest secondary anisotropy at the arcminute scale is due to the tSZ effect. The tSZ effect is caused by the thermal motion of electrons mainly from hot-ionized gas in galaxy clusters whereas the kSZ effect is attributed

*E-mail: D.Munshi@sussex.ac.uk
[1] http://www.cfhtlens.org/
[2] http:/www.rssd.esa.int/index.php?project=planck

to the bulk motion of electrons in an ionized medium (Sunyaev & Zeldovich 1972, 1980). The tSZ can be separated from CMB maps using spectral information. Along with lensing of CMB, the kSZ is the most dominant secondary contribution at arcminute scale after the removal of tSZ, as primary CMB is sub-dominant due to the Silk-damping (Ostriker & Vishniac 1986; Vishniac 1987; Jaffe & Kamionkowski 1998; Ma & Fry 2000; Valageas, Balbi & Silk 2001).

The tSZ and kSZ effects are both promising probes of the ionized fractions of the baryons. Majority of tSZ effect is caused by electrons in virialized collapsed objects (Hernández-Montegudo et al. 2006; White, Song & Percival 2009). The overdensity in these regions is considerably high, $\delta > 100$. The missing baryons however are more likely to reside in filaments with moderate overdensity and lower temperature and hence unlikely to be probed efficiently by tSZ. Interestingly, the kSZ is linked to the peculiar velocity which is sensitive to large-scale potential and less likely to be sensitive to individual collapsed objects. It is also less sensitive to the thermal state and can probe contributions from individual baryonic components in a relatively unbiased way (Génova-Santos et al. 2009). For previous studies of kSZ effect from WHIMs see e.g. Atrio-Barandela, Mucket & Génova-Santos (2008) and Génova-Santos et al. (2009). The methods for extracting the kSZ which we present here are free from systematics that one might encounter when trying to detect it using the CMB two-point auto correlation function or equivalently the power-spectral analysis.

The kSZ signal is not only extremely weak; it also lacks any spectral feature (Ma & Fry 2000, 2002; Zhang, Pen & Trac 2004; Shaw, Rudd & Nagai 2012) and is overwhelmed by the primary CMB below $\ell \approx 3000$. The kSZ effect dominates at the damping tail of the primary beyond $\ell \geq 3000$ only at $\nu = 217$ GHz where the dominant *secondary* contribution from the non-relativistic tSZ effect vanishes. Contamination from dusty star-forming galaxies can also further complicate detection of kSZ effect (Hall et al. 2010). Use of non-Gaussianity has been suggested as possible method to separate kSZ from confusion due to lensing of CMB (Castro 2004; Riquelme & Spergel 2007).

Being a CMB secondary anisotropy, the kSZ effect includes projected contributions from various independent components and lacks any redshift information. It is a projection of electron momentum along the line of sight (LoS). Lack of redshift information means it is impossible to separate individual contribution such as from a *patchy* reionization history, which is expected to contribute significantly and thus can in principle bias any estimates of missing baryons. The tight cross-correlation of tSZ and galaxy densities has been probed in the literature in detail (Zhang & Pen 2001; Shao et al. 2011b). However such a cross-correlation vanishes due to the vectorial (spin-1) nature of the kSZ. To circumvent this problem various options have currently been tried, e.g. using higher order cumulant correlators (Dore, Hennawi & Spergel 2004; DeDeo, Spergel & Trac 2005) or tomographic cross-correlation with galaxy redshift surveys (Shao et al. 2011a). Cross-correlation with other tracers of low-redshift large-scale structure e.g. intensity mapping from future 21 cm surveys has also been considered (Chang et al. 2008).

The recently proposed technique dubbed kSZ *tomography* (Ho, Dedeo & Spergel 2009; Shao et al. 2011a), involves reconstructing the galaxy peculiar velocity field from spectroscopic redshift surveys and including galaxy number density and other redshift dependent pre-factors. Notice that bulk flows on scales of $\geq$1 Gpc and the pairwise velocity dispersion have been observed (Kashlinsky, Atrio-Barandela & Ebeling 2011; Kashlinsky et al. 2008; Kashlinsky et al. 2010; Hand et al. 2012; Morkczkowski et al. 2012). However, there is no broad agreement on the coherent bulk flow on very large scale ($\sim$Gpc scale), and it is still controversial based on recent observations, see e.g. Mody & Hajian (2012). The reconstructed momentum field has very similar directional dependence as the true kSZ effect. Thus the cross-correlation of these two can be used as an indicator for the kSZ contribution to CMB maps. With redshift space binning it is also possible to study evolution of kSZ contribution as a function of redshift. This method can be useful in separating out not only the primary CMB from kSZ but also various contribution such as the contribution from patchy reionization. A high value for the signal to noise ratio $(S/N) = 50$ was estimated using Planck[3] and the BigBoss (currently MS-DESI or Mid-Scale Dark Energy Spectroscopic Instrument)[4] survey. Notice that similar tomographic reconstruction was also proposed for tSZ (Shao et al. 2011b) as was recently extended to 3D recently (Pratten & Munshi 2014).

In recent years, there has been significant progress in extracting survey information using three-dimensional spherical Fourier–Bessel (sFB) decomposition of galaxy surveys which goes beyond a tomographic treatment (Ballinger, Heavens & Taylor 1995; Heavens & Taylor 1995; Pratten & Munshi 2012, 2013). The formalism involves expanding the galaxy density field in a sFB expansion. The formalism was found extremely useful in analysing weak lensing data in 3D (Heavens 2003; Castro, Heavens & Kitching 2005; Munshi et al. 2011b). Going beyond the tomographic cross-correlation in this paper we use a 3D treatment to reconstruct the kSZ from galaxy surveys. This is in line with the reconstruction technique developed for tSZ by Pratten & Munshi (2014) using a 3D sFB decomposition.

Spectroscopic galaxy redshift surveys, such as LAMOST,[5] BOSS,[6] BigBOSS, SKA,[7] Euclid[8] and JDEM/ADEPT[9] will map the galaxy distribution in 3D. These surveys will have overlap in terms of observed regions of the sky with ongoing CMB surveys, e.g. ACT,[10] SPT[11] and Planck. It is possible to recover the velocity fields from such surveys and construct an estimator in 3D that can be correlated with CMB maps to reconstruct the distribution of ionized gas whose bulk velocity is causing the kSZ.

[3] http://www.cosmos.esa.int/web/planck
[4] http://www.bigboss.lbl.org.gov/index.html
[5] http://www.lamost.org/website/en
[6] http://www.cosmology.lbl.org.gov/BOSS
[7] http://www.skatelescope.org
[8] http://www.sci.esa.int/euclid
[9] http://www.jdem.gsfc.nasa.gov/
[10] http://www.physics.princeton.edu/act
[11] http://www.southpole.uchicago.edu

The primary aim of this paper is to disentangle the low-redshift (late-time) contribution to kSZ effect and that from a rather poorly understood reionization history. This will allow us to use future kSZ surveys in constraining the interaction of dark energy (DE) and dark matter (DM) using the kSZ effect as such a non-gravitational coupling in the dark sector can significantly affect the expansion history of the Universe as well as growth of structure (Xu et al. 2013). Indeed various modified gravity theories that affect the growth rate and power spectrum of perturbation can also be constrained using kSZ effect. The results presented here will be relevant to extending studies of kSZ in constraining radial inhomogeneities in Lemaitre–Tolman–Bondi cosmologies (Bull, Clifton & Ferreira 2011) or dark flow (Zhang 2010).

The current upper limit on the KSZ power spectrum from the Atacama Cosmology Telescope (ACT) is 8.6 μK^2 at $\ell = 3000$. The upper limits from the South Pole Telescope (SPT) is 2.8 μK^2 at $\ell = 3000$. Most recently George et al. (2015) reported $\mathcal{D}^{\rm kSZ}_{\ell=3000} = (2.9 \pm 1.3)\,\mu{\rm K}^2$ ($\mathcal{D}^{\rm kSZ}_{\ell} = \ell(\ell+1)\mathcal{C}^{\rm kSZ}_{\ell}/2\pi$). These upper limits depend on the reionization history, modelling of cosmic infrared background, tSZ contribution and separation of the kSZ effect into homogeneous and patchy components. Using arcminute resolution maps from ACT and BOSS statistical evidence was presented for motion of galaxy clusters through their kSZ signature (Hand et al. 2012). The foreground-cleaned maps from Planck nominal mission data were used to achieve a 1.8–2.5σ detections of the kSZ signal. This was achieved by estimating the pairwise momentum of the kSZ temperature fluctuations at the positions of the Central Galaxy Catalogue samples extracted from Sloan Digital Sky Survey (DR7) data (Planck Collaboration XXXVII 2016). In the same study, data from *WMAP*[12] i.e. *WMAP*-9 yr W band data a detection of 3.3σ was also reported.

The best constraints on reionization history are likely to result from redshifted 21-cm experiments with low-frequency radio interferometers GMRT[13] (Paciga et al. 2011), LOFAR[14] (Harker et al. 2010), MWA[15] (Lonsdale et al. 2009) and PAPER(Parson et al. 2010). The nearinfrared background measurements with CIBER[16] and AKARI[17] will also provide valuable clues to reionization history. In addition, ground-based observations of high-redshift QSO, galaxies and GRBs too provide important clues to reionization history (Ouchi et al. 2010; Cucchiara et al. 2011; Kashikawa et al. 2011; Mortlock et al. 2011).

The plan of this paper is as follows. The Section 2 is devoted to introducing our notation. In Section 3, we motivate a 3D analysis for kSZ reconstruction. In Section 4, we derive the expressions for 3D power spectrum. In Section 5, we present how to construct the tomographic and 2D maps and power spectrum from 3D information. The Section 6 gives analytical expression for S/N of 3D reconstruction. The Section 7 is devoted to the discussion of the two power spectra $P_{q\perp}$ and $P_{q\parallel}$ which are used as an input for the kSZ power-spectra computation. The Section 4.2 is reserved for discussion of our results. Finally, the conclusions are presented in Section 9. We have included the discussions of issues related to the partial sky coverage in Appendix.

The results presented here will be useful in studies of *bulk flow* which will clearly benefit from more resolved radial modes that can improve their S/N ratio.

2 A NOTE ON NOTATIONS

In this section, we introduce our cosmological notations for the kSZ effect that will be used later.

$$ds^2 = -c^2dt^2 + a^2(r)\left(dr^2 + d_{\rm A}^2(r)(\sin^2\vartheta\, d\vartheta^2 + d\varphi^2)\right); \tag{1}$$

$$d_{\rm A}(r) = \lambda_{\rm H}\frac{\sin_{\rm K}(|\Omega_{\rm K}|^{1/2}r/\lambda_{\rm H})}{|\Omega_{\rm K}|^{1/2}}; \quad \lambda_{\rm H} = c\,H_0^{-1}; \tag{2}$$

$$r(z) = \lambda_{\rm H}\int_0^z \frac{dz'}{E(z')}; \qquad E(z) = \frac{H(z)}{H_0} = \sqrt{\Omega_\Lambda + \Omega_{\rm K}(1+z)^2 + \Omega_M(1+z)^3}. \tag{3}$$

We will use the line element ds defined above. Throughout c will denote speed of light and will be set to unity. In our notation, $d_{\rm A}(r)$ is the comoving angular diameter distance at a (comoving) radial distance r and can be expressed in terms of the curvature density parameter $\Omega_{\rm K} = 1 - \Omega_{\rm M} - \Omega_\Lambda$; $\rm H_0 = 100\,\mathit{h}\ km\,s^{-1}\,Mpc^{-1}$ is the Hubble constant; $\Omega_{\rm M}$ is the current non-relativistic matter density in units of critical density and Ω_Λ is current contribution of cosmological constant to the critical density. In equation (2) $\sin_{\rm K}$ represents sinh if $\Omega_{\rm K} < 0$ or sin if $\Omega_{\rm K} > 0$; if $\Omega_{\rm K} = 0$, then $d_{\rm A}(r) = r$. We will denote the linear growth factor as $D_+(r)$ defined such that the Fourier transform of the overdensity field grows as $\delta(k\boldsymbol{k}, r) = D_+(r)\delta(\boldsymbol{k}, 0)$ is given by:

$$D_+(z) = \frac{H(z)}{H_0}\int_z^\infty dz'(1+z')\left[H(z')\right]^{-3} \Big/ \int_0^\infty dz''(1+z'')\left[H(z'')\right]^{-3}. \tag{4}$$

The particular cosmology that we will adopt for numerical study is specified by the following parameter values (to be introduced later): $\Omega_\Lambda = 0.741,\ h = 0.72,\ \Omega_{\rm b} = 0.044,\ \Omega_{\rm CDM} = 0.215,\ \Omega_{\rm M} = \Omega_{\rm b} + \Omega_{\rm CDM},\ n_{\rm s} = 0.964,\ w_0 = -1,\ w_{\rm a} = 0,\ \sigma_8 = 0.803,\ \Omega_\nu = 0.$

[12] http://map.gsfc.nasa.gov/
[13] http://gmrt.ncra.tifr.res.in/
[14] http://www.lofar.org/
[15] http://www.mwatelescope.org/
[16] http://physics.ucsd.edu/ bkeating/CIBER.html
[17] http://irsa.ipac.caltech.edu/Missions/akari.html

3 LATE-TIME KSZ

The cosmic ionized transverse momentum can be studied as a temperature fluctuation in the CMB maps. The LoS component of the momentum of electrons in the ionized IGM introduces temperature fluctuation via the Doppler effect also known as the kSZ. The contribution from the longitudinal component suffers cancellation due to contribution from successive troughs and crests (Vishniac 1987). The measured kSZ power spectrum is the sum over contribution from the epoch of reionization (EoR) and the post-reionization or late-time kSZ contribution. Inhomogeneity in the ionization fraction during EoR gives a large boost to the kSZ power spectrum. The physics that determines the *patchy* or inhomogeneous reionization is complex. Analytical (Gruzinov & Hu 1998; Santos et al. 2003), semi-analytical(McQuinn et al. 2005; Zahn et al. 2011; Mesinger, McQuinn & Spergel 2012; Battaglia et al. 2013) and numerical *N*-body simulations coupled with radiative transfer (Iliev et al. 2007; Park et al. 2013) are often used to understand various aspects. The contribution from *late-time* kSZ is relatively easier to model and will be the main focus of this paper.

Inhomogeneity in electron density, defined by the density contrast $\delta_{\rm e}(\boldsymbol{r})$ and peculiar velocity $\boldsymbol{v}(\boldsymbol{r})$ as well as in ionization fraction $\chi_{\rm e}$ can all lead to secondary fluctuation in the CMB temperature $\Theta(\hat{\boldsymbol{\Omega}}) \equiv \delta T(\hat{\boldsymbol{\Omega}})/T_0$. The specific ionized momentum field $\boldsymbol{q}(\boldsymbol{r})$ at $\boldsymbol{r} = (r, \hat{\boldsymbol{\Omega}}) = (r, \vartheta, \varphi)$ is given by (Gruzinov & Hu 1998; Knox, Scoccimarro & Dodelson 1998):

$$\boldsymbol{q}(\boldsymbol{r}) \equiv \chi_{\rm e}(r)\boldsymbol{v}(\boldsymbol{r})(1+\delta_{\rm e}(\boldsymbol{r})). \tag{5}$$

The ionized fraction $\chi_{\rm e}$ is defined in terms of electron density $n_{\rm e}$ and number density of Hydrogen(H) and Helium(He) atoms denoted as $n_{\rm H}$ and $n_{\rm He}$, respectively i.e. $\chi_{\rm e} = n_{\rm e}/(n_{\rm H} + 2n_{\rm He})$. For post-reionization or late-time kSZ computation we will set $\chi_{\rm e} = 1$. If we assume that hydrogen reionization was finished at $z = 6$ and He II reionization occurred instantaneously at $z = 3$ we will have $\chi_{\rm e} = 0.93$ for $3 < z < 6$ and $\chi_{\rm e} = 1$ for $z < 3$. Our reconstruction technique is based on local large-scale tracers which typically cover the redshift range $z < 3$ which justifies our choice of $\chi_{\rm e} = 1$. Modelling of the post-reionization signal is simpler because the IGM is fully ionized and $\chi_{\rm e}$ does not fluctuate to a good approximation: $\boldsymbol{q}(\boldsymbol{r}) \equiv \boldsymbol{v}(\boldsymbol{r})(1+\delta_{\rm e}(\boldsymbol{r}))$. We thus need to model the electron density $\delta_{\rm e}$ and velocity $\boldsymbol{v}$ fluctuation of gas. The velocity filed is purely longitudinal in the quasi-linear regime. In general the baryonic density contrast $\delta_{\rm e}(\boldsymbol{r})$ can be different from the DM density especially on scales smaller than the Jeans-length scale. Indeed the shock-heated gas will be less clustered than the underlying DM due to baryonic pressure. This effect can have modest impact on kSZ power spectrum at $\ell = 3000$. Star formation converts gas into stars thus reducing the kSZ effect further; gas-cooling and star formation can reduce the kSZ effect up to 33 per cent. These effects can only be dealt with using numerical simulations. For this paper we will assume that the baryons trace the DM on the scales of interest which are much larger than the Jeans length scale.

The kSZ is given by the transverse momentum field, hence is a vector mode which can be described also as a spin-1 field.

$$\Theta(\hat{\boldsymbol{\Omega}}) \equiv \frac{\Delta {\rm T}(\hat{\boldsymbol{\Omega}})}{{\rm T}_0} = \int_0^{z_{\rm LSS}} dr\, \phi(r)\Psi(\boldsymbol{r}); \quad \Psi(\boldsymbol{r}) = \frac{\hat{\boldsymbol{\Omega}}\cdot\boldsymbol{q}(\boldsymbol{r})}{c}; \tag{6}$$

$$\phi(r) = -\frac{\sigma_{\rm T}\chi_{\rm e}\bar{n}_{\rm e,0}}{c}\frac{{\rm e}^{-\tau(r)}}{a^2}. \tag{7}$$

The projected momentum $\Psi(\boldsymbol{r})$ is the 3D momentum projected along the LoS direction at a distance $\boldsymbol{r}$. Here $\hat{\boldsymbol{\Omega}}$ is the unit vector along the LoS direction, r is the comoving distance along the LoS direction. We also note that the optical depth τ due to Thompson scattering can be expressed as:

$$d\tau = c\, n_{\rm e}(z)\, \sigma_{\rm T}\, \frac{dt}{dz}\, {\rm d}z, \tag{8}$$

where τ is the optical depth due to Thompson scattering integrated from $z = 0$ to surface of last scattering at $z \sim 10^3$; $\sigma_{\rm T} = 0.665\,245\,74 \times 10^{-24}\,{\rm cm}^2$ is the Thompson scattering cross-section for electrons and $\bar{n}_{\rm e,0} = \bar{n}_{\rm H} + 2\bar{n}_{\rm He}$. The visibility function $g(t)$ is defined as:

$$g(t) \equiv -\dot{\tau}\,\exp[-\tau(t)] = c\,\sigma_{\rm T}\,n_{\rm e}(t)\,\exp[-\tau(t)]. \tag{9}$$

In this paper, we propose to construct a 3D estimator $\hat{\Theta}(\boldsymbol{r})$ for kSZ induced temperature fluctuation in CMB maps. The corresponding projected $\hat{\Theta}(\hat{\boldsymbol{\Omega}})$ and tomographic estimators $\hat{\Theta}_i(\hat{\boldsymbol{\Omega}})$ can be computed using suitable LoS integration. We construct $\boldsymbol{q}(\mathbf{r})$ from 3D spectroscopic surveys:

$$\hat{\Theta}(\boldsymbol{r}) = \phi(r)\Psi(\boldsymbol{r}) \qquad \hat{\Theta}(\hat{\boldsymbol{\Omega}}) = \int_0^{z_{\rm LSS}} dr\ \hat{\Theta}(\boldsymbol{r}); \quad \hat{\Theta}_i(\hat{\boldsymbol{\Omega}}) = \int_{z_i}^{z_{i+1}} dr\ \hat{\Theta}(\boldsymbol{r}). \tag{10}$$

The weighted momentum field $\boldsymbol{q}(\boldsymbol{r})$ is constructed to have the same directional dependence as the kSZ effect and thus should cross-correlate with the CMB maps and help us to extract the kSZ component of CMB. Similar correlations have been studied before in tomographic bins (Ho et al. 2009; Shao et al. 2011a) where the radial integral was restricted to a particular bin. Our approach is to go beyond the tomographic description and constructs the kSZ effect in 3D. The cross-correlation technique has several advantages over the auto correlation technique. Due to the use of 3D template that involves matching characteristic directional dependence, it is possible to avoid contamination from tSZ, dusty star-forming galaxies, as well as from the Primary CMB. This is rather important given the weak nature of the kSZ signal and overwhelming systematic error. The redshift information in our estimator also allows separating out the kSZ contributions from patchy reionization and late-time kSZ effect. Typically the high number density of galaxy ensures a higher signal-to-noise ratio for such an estimator. Similar 3D techniques was be used to reconstruct the tSZ effect (Pratten & Munshi 2014).

4 3D ESTIMATORS FOR LATE-TIME KSZ

Spherical coordinates are a natural choice for the analysis of cosmological data sets as, by an appropriate choice of coordinates, we can place an observer at the origin of the analysis. Future large-scale surveys will provide an unprecedented level of detail by generating extended sky maps with large radial coverage. We therefore require a simultaneous treatment of the extended radial coverage and the spherical sky geometry. For this problem the sFB expansion is a natural basis for the analysis of cosmological random fields. The sFB formalism has seen an increased use in the literature over the past few years, for example it has been used in: weak lensing studies (Heavens 2003; Castro et al 2005; Heavens, Kitching & Taylor 2006; Munshi, Heavens & Coles 2011; Kitching, Heavens & Miller 2011; Ayaita, Schaeffer & Weber 2012), redshift space distortions (Heavens & Taylor 1995; Pratten & Munshi 2013; Munshi et al. 2015), relativistic effects (February, Clarkson & Maartens 2013; Yoo & Desjacques 2013) and studies of baryon acoustic oscillations (Rassat & Refregier 2012; Grassi & Schaefer 2014; Pratten & Munshi 2013).

The forward and inverse sFB decomposition of the 3D field $\alpha(\boldsymbol{r})$ is defined as:

$$\alpha_{\ell m}(k) = \sqrt{\frac{2}{\pi}} \int d^3\boldsymbol{r}\; k\; j_\ell(kr)\; Y^*_{\ell m}(\hat{\boldsymbol{\Omega}})\; \alpha(\boldsymbol{r}); \tag{11}$$

$$\alpha(\boldsymbol{r}) = \sqrt{\frac{2}{\pi}} \int k\mathrm{d}k \sum_{\ell m} \alpha_{\ell m}(k)\; j_\ell(kr) Y^*_{\ell m}(\hat{\boldsymbol{\Omega}}); \quad \boldsymbol{r} \equiv (r, \hat{\boldsymbol{\Omega}}); \tag{12}$$

$$\hat{\boldsymbol{\Omega}} = (\cos\vartheta\,\sin\varphi, \sin\vartheta\,\sin\varphi, \cos\varphi). \tag{13}$$

The basis function for the sFB expansion is an eigen function of the Laplacian operator $\sqrt{\frac{2}{\pi}} k j_\ell(kr) Y_{\ell m}(\hat{\boldsymbol{\Omega}})$ in spherical co-ordinates. Here, k denotes the radial wavenumber and $\{\ell m\}$ denotes the azimuthal wave numbers; $Y_{\ell m}$ are the spherical harmonics and j_ℓ are the spherical Bessel functions. In general the continuous integral over r can be a replaced with a discrete sum over galaxy position i.e. effectively replacing the galaxy density with a sum over Dirac's delta functions $\alpha(\boldsymbol{r}) = \delta_{\rm D}(\boldsymbol{r} - \boldsymbol{r}_i)$ that are non-zero at galaxy position $\boldsymbol{r}_i$. Throughout results from an all-sky experiment will be presented. For flat-sky results relevant for small patch of the sky the spherical harmonics are replaced by exponential function.

To relate the radial distance r with the observed redshift of galaxies z a background cosmology needs to be assumed. The expressions derived above is technically valid for a flat Universe. To relax this assumption we have to replace the spherical Bessel functions with hyperspherical Bessel functions. To analyse realistic data weights are introduced. Such arbitrary masks will be incorporated using a 3D pseudo-$\mathcal{C}_\ell$ approach.

Our aim is to relate the 3D harmonics of $\Theta_{\ell m}(k)$ with the underlying perturbations in specific ionized momentum field $\boldsymbol{q}(r)$ defined in equation (5). To this end, we will Fourier decompose the momentum vector $\boldsymbol{q}(\boldsymbol{r})$ whose Fourier components are $\tilde{\mathbf{q}}(\boldsymbol{k})$:

$$\tilde{\mathbf{q}}(\boldsymbol{k}) = \int d^3\boldsymbol{r}\; \boldsymbol{q}(\boldsymbol{r})\; \mathrm{e}^{\mathrm{i}\mathbf{k}\cdot\boldsymbol{r}}. \tag{14}$$

We will separately deal with the contribution to kSZ from longitudinal $\tilde{\mathbf{q}}_\parallel(\boldsymbol{k})$ and transverse $\tilde{\mathbf{q}}_\perp(\boldsymbol{k})$ components of $\tilde{\mathbf{q}}(\boldsymbol{k})$ also known as the divergence free (curl) component of $\boldsymbol{q}$ i.e. $\boldsymbol{q}_\perp$ and curl free (divergence) components. They are defined using the following expressions:

$$\tilde{\mathbf{q}}_\parallel(\boldsymbol{k}) = \tilde{\mathbf{q}}(\boldsymbol{k}) - \tilde{\mathbf{q}}_\perp(\boldsymbol{k}); \tag{15}$$

$$\tilde{\mathbf{q}}_\perp(\boldsymbol{k}) = \hat{\boldsymbol{\Omega}}_k[\tilde{\mathbf{q}}(\boldsymbol{k}) \cdot \hat{\boldsymbol{\Omega}}_k]; \qquad \boldsymbol{k} = (k, \hat{\boldsymbol{\Omega}}_k). \tag{16}$$

The two power spectra $P_{q_\perp}(k; r, r')$ and $P_{q_\parallel}(k; r, r')$ for $\tilde{\mathbf{q}}_\parallel(\boldsymbol{k}; r)$ and $\tilde{\mathbf{q}}_\perp(\boldsymbol{k}; r)$ are defined as follows:

$$\langle \tilde{\mathbf{q}}_\perp(\boldsymbol{k}; r) \tilde{\mathbf{q}}_\perp(\boldsymbol{k}'; r') \rangle = (2\pi)^3 P_{q_\perp}(k;\, r, r') \delta_{3\rm D}(\boldsymbol{k} - \boldsymbol{k}'); \tag{17}$$

$$\langle \tilde{\mathbf{q}}_\parallel(\boldsymbol{k}; r) \tilde{\mathbf{q}}_\parallel(\boldsymbol{k}'; r') \rangle = (2\pi)^3 P_{q_\parallel}(k;\, r, r') \delta_{3\rm D}(\boldsymbol{k} - \boldsymbol{k}'). \tag{18}$$

The expressions for $P_{q_\perp}$ and $P_{q_\parallel}$ in terms of the matter power spectrum $P_{\delta\delta}$ will be presented in Section 7.

We will next deal with the contribution to kSZ from the longitudinal and transverse components independently. First we express the $\Theta(\hat{\boldsymbol{\Omega}})$ in terms of the Fourier components of $\Psi(\boldsymbol{r})$ i.e. $\tilde{\Psi}(\boldsymbol{k})$. Following the same convention for Fourier transform as described in equation (14):

$$\Theta(\hat{\boldsymbol{\Omega}}) = \int\; dr\; \phi(r) \int \frac{d^3k}{(2\pi)^3}\; \tilde{\Psi}(\boldsymbol{k}, \boldsymbol{r})\; \mathrm{e}^{-\mathrm{i}\,\boldsymbol{k}\cdot\boldsymbol{r}}. \tag{19}$$

We will write $\tilde{\Psi} = \tilde{\Psi}^\parallel + \tilde{\Psi}^\perp$ where $\tilde{\Psi}^\parallel$ depends only on $\tilde{\mathbf{q}}_\parallel$ and $\tilde{\Psi}^\perp$ on $\tilde{\mathbf{q}}_\perp$. Contribution to the total $\Theta(\hat{\boldsymbol{\Omega}})$ can now be broken into two parts namely $\Theta^\parallel(\hat{\boldsymbol{\Omega}})$ and $\Theta^\perp(\hat{\boldsymbol{\Omega}})$ with $\Theta(\hat{\boldsymbol{\Omega}}) = \Theta^\parallel(\hat{\boldsymbol{\Omega}}) + \Theta^\perp(\hat{\boldsymbol{\Omega}})$.

$$\Theta^\parallel(\hat{\boldsymbol{\Omega}}) \equiv \int\; dr\; \Theta^\parallel(\boldsymbol{r}); \qquad \Theta^\parallel(\boldsymbol{r}) \equiv \phi(r) \int \frac{d^3k}{(2\pi)^3} \tilde{\Psi}^\parallel(\boldsymbol{k}, r) \mathrm{e}^{-\mathrm{i}\mathbf{k}\cdot\boldsymbol{r}}; \qquad \tilde{\Psi}^\parallel(\boldsymbol{k}, r) = \left[x\; \tilde{\mathbf{q}}_\parallel(\boldsymbol{k}, r)\right]; \tag{20}$$

$$\Theta^{\perp}(\hat{\mathbf{\Omega}}) = \int dr\ \Theta^{\perp}(\boldsymbol{r}); \qquad \Theta^{\perp}(\boldsymbol{r}) \equiv \phi(r) \int \frac{d^3k}{(2\pi)^3} \tilde{\Psi}^{\perp}(\boldsymbol{k}, r) \mathrm{e}^{-\mathrm{i}\mathbf{k}\cdot\boldsymbol{r}}; \quad \tilde{\Psi}^{\perp}(\boldsymbol{k}, r) = [\cos(\varphi_q - \varphi)\sqrt{(1-x^2)}\ \ \tilde{\mathbf{q}}_{\perp}(\mathbf{k}, r)]. \tag{21}$$

We have defined $x = [\hat{\mathbf{\Omega}}_{\rm k} \cdot \hat{\mathbf{\Omega}}]$. Throughout we will denote unit vector in real space as $\hat{\mathbf{\Omega}}$ and as $\hat{\mathbf{\Omega}}_{\rm k}$ in the Fourier domain.

Using a 3D spherical harmonic decomposition of $\Theta^{\parallel}(\boldsymbol{r})$ and $\Theta^{\perp}(\boldsymbol{r})$, denoted as $\Theta^{\parallel}_{\ell m}(k)$ and $\Theta^{\perp}_{\ell m}(k)$, respectively, corresponding projected (2D) harmonics $\Theta^{\parallel}_{\ell m}$ and $\Theta^{\perp}_{\ell m}$ are obtained by spherical harmonics decomposition of the respective 2D analogues i.e. $\Theta^{\parallel}$ and $\Theta^{\perp}$. We will construct two power 3D spectra $\mathcal{C}^{\perp}_{\ell}(k_1, k_2)$ and $\mathcal{C}^{\parallel}_{\ell}(k_1, k_2)$ similarly to $\mathcal{C}^{\perp}_{\ell}$ and $\mathcal{C}^{\parallel}_{\ell}$ in 2D. We will also consider cross-correlation of our 3D harmonics with the corresponding 2D harmonics to construct $\mathcal{C}^{\parallel}_{\ell}(k)$ and $\mathcal{C}^{\perp}_{\ell}(k)$. We will express these power spectra in terms of $P_{q_{\parallel}}$ and $P_{q_{\perp}}$.

4.1 Evaluating the perpendicular components of the 3D sFB covariance $\mathcal{C}^{\perp}_{\ell}(k, k')$ and the projected 2D power spectrum $\mathcal{C}^{\perp}_{\ell}(k)$

In order to compute the contribution from the *transverse* component we will use the definition of $\Theta_{\perp}(\boldsymbol{r})$ from equation (21) to express the power spectrum $\mathcal{C}^{\perp}_{\ell}$ in terms of $P_{q\perp}$:

$$\Theta^{\perp}(\boldsymbol{r}) \equiv \phi(r) \int \frac{d^3\boldsymbol{k}'}{(2\pi)^3} \tilde{\Psi}^{\perp}(\boldsymbol{k}', \boldsymbol{r}); \tag{22}$$

$$\tilde{\Psi}^{\perp}(\boldsymbol{k}, \boldsymbol{r}) = \cos(\varphi_q - \varphi)\sqrt{1-x^2}\ \ \tilde{\mathbf{q}}_{\perp}(\boldsymbol{k}, r)\, \mathrm{e}^{-\mathrm{i}\mathbf{k}\cdot\boldsymbol{r}}. \tag{23}$$

Next, we use the following definitions for $Y_{1\pm1}(\hat{\mathbf{\Omega}})$:

$$Y_{1,-1}(\hat{\mathbf{\Omega}}) = \frac{1}{2}\sqrt{\frac{3}{2\pi}}\ \sin\vartheta\ \mathrm{e}^{-\mathrm{i}\varphi}; \qquad Y_{1,1}(\hat{\mathbf{\Omega}}) = -\frac{1}{2}\sqrt{\frac{3}{2\pi}}\ \sin\vartheta\ \mathrm{e}^{\mathrm{i}\varphi}; \tag{24}$$

to express the trigonometric function in terms of lower order spherical harmonics[18] $Y_{\ell m}(\hat{\Omega})$:

$$\cos\varphi \sin\vartheta = \sqrt{\frac{2\pi}{3}}[Y_{1,-1}(\hat{\mathbf{\Omega}}) - Y_{1,1}(\hat{\mathbf{\Omega}})]. \tag{25}$$

We will also be using the Rayleigh expansion of plane wave in terms of spherical wave:

$$\mathrm{e}^{-\mathrm{i}\mathbf{k}\cdot\boldsymbol{r}} = 4\pi \sum_{\ell m} (-i)^{\ell}\, j_{\ell}(kr) Y_{\ell m}(\hat{\mathbf{\Omega}}) Y_{\ell m}(\hat{\mathbf{\Omega}}_{\rm k}). \tag{26}$$

Choosing the unit vector $\hat{\mathbf{\Omega}}_{\rm k}$ along the z direction, $\hat{\mathbf{\Omega}}_{\rm k} = \hat{\boldsymbol{z}}$ we can replace $Y_{\ell \rm m}(\hat{\mathbf{\Omega}}_{\rm k}) = \delta_{\rm m0}\sqrt{\frac{\Sigma_{\ell}}{4\pi}}$ with $\Sigma_{\ell} = 2\ell + 1$. Using expressions from equation (25) we can write:

$$\begin{aligned}\tilde{\Psi}^{\perp}(k\hat{\boldsymbol{z}}; \boldsymbol{r}) &= 4\pi\sqrt{\frac{2\pi}{3}}[Y_{1,-1}(\hat{\mathbf{\Omega}}) - Y_{1,1}(\hat{\mathbf{\Omega}})]\ \tilde{\mathbf{q}}_{\perp}(\boldsymbol{k}, r) \sum_{\ell' m'} (-i)^{\ell'}\ j_{\ell'}(kr)\, Y_{\ell' m'}(\hat{\mathbf{\Omega}})\, Y_{\ell' m'}(\hat{\mathbf{\Omega}}_{\rm k}) \\ &= \sqrt{4\pi}\ \sqrt{\frac{2\pi}{3}}\ [Y_{1,-1}(\hat{\mathbf{\Omega}}) - Y_{1,1}(\hat{\mathbf{\Omega}})]\ \tilde{\mathbf{q}}_{\perp}(\boldsymbol{k}, r) \sum_{\ell'} (-i)^{\ell'}\ \sqrt{\Sigma_{\ell'}}\ j_{\ell'}(kr)\ Y_{\ell' 0}(\hat{\mathbf{\Omega}}).\end{aligned} \tag{27}$$

We will express the overlap-integrals involving three spherical harmonics in terms of 3j symbols:

$$\tilde{\Psi}^{\perp}_{\ell m}(k\hat{\boldsymbol{z}}, r) = \sqrt{4\pi}\sqrt{\frac{2\pi}{3}}\tilde{\mathbf{q}}_{\perp}(k\hat{\boldsymbol{z}}, r) \sum_{\ell'}\ (-i)^{\ell'}\ j_{\ell'}(k\, r)\ \sqrt{\Sigma}_{\ell'}\ \int\ d\hat{\mathbf{\Omega}}\ Y_{\ell' 0}(\hat{\mathbf{\Omega}})\ [Y_{1,-1}(\hat{\mathbf{\Omega}}) - Y_{1,1}(\hat{\mathbf{\Omega}})]\ Y^{*}_{\ell m}(\hat{\mathbf{\Omega}}); \tag{28}$$

$$\begin{aligned}&= \sqrt{4\pi}\sqrt{\frac{2\pi}{3}}\tilde{\mathbf{q}}_{\perp}(k\hat{\boldsymbol{z}}, r) \sum_{\ell'} (-i)^{\ell'}\ I_{\ell,\ell',1}\ j_{\ell'}(kr)\sqrt{\Sigma}_{\ell} \begin{pmatrix} \ell & \ell' & +1 \\ 0 & 0 & 0 \end{pmatrix} \\ &\quad \times \left[\begin{pmatrix} \ell & \ell' & +1 \\ -m & 0 & -1 \end{pmatrix} - \begin{pmatrix} \ell & \ell' & +1 \\ -m & 0 & +1 \end{pmatrix} \right].\end{aligned} \tag{29}$$

The 3j symbols are defined through the *Gaunt* integral:

$$\int\ d\hat{\mathbf{\Omega}}\ Y_{\ell_1 m_1}(\hat{\mathbf{\Omega}})\ Y_{\ell_2 m_2}(\hat{\mathbf{\Omega}})\ Y_{\ell_3 m_3}(\hat{\mathbf{\Omega}}) = I_{\ell_1,\ell_2,\ell_3} \begin{pmatrix} \ell_1 & \ell_2 & \ell_3 \\ 0 & 0 & 0 \end{pmatrix} \begin{pmatrix} \ell_1 & \ell_2 & \ell_3 \\ m_1 & m_2 & m_3 \end{pmatrix}; \tag{30}$$

$$I_{\ell_1,\ell_2,\ell_3} = \sqrt{\frac{\Sigma_{\ell_1}\Sigma_{\ell_2}\Sigma_{\ell_3}}{4\,\pi}}. \tag{31}$$

[18] http://mathworld.wolfram.com/SphericalHarmonic.html

For various symmetry properties of 3*j* symbols see e.g. Edmonds (1996). Notice, only $m = \pm 1$ multipoles contribute as the 3*j* symbols need to satisfy the condition $m_1 + m_2 + m_3 = 0$. The first term in the equation (29) contributes for $m = -1$ and the second term contributes for $m = 1$.

We will use the following identities in our derivation to evaluate the special cases of the 3j symbols that appear:

$$\begin{pmatrix} \ell_1 & \ell_2 & \ell_3 \\ 0 & 0 & 0 \end{pmatrix} = (-1)^{\ell} \sqrt{\frac{(2\ell - 2\ell_1)!(2\ell - 2\ell_2)!(2\ell - 2\ell_3)!}{(2\ell + 1)!}} \frac{\ell!}{(\ell - \ell_1)!(\ell - \ell_2)!(\ell - \ell_3)!}; \qquad \ell_1 + \ell_2 + \ell_3 = 2\ell$$
$$= 0; \qquad \ell_1 + \ell_2 + \ell_3 = 2\ell + 1. \tag{32}$$

$$\begin{pmatrix} \ell_1 & \ell_2 & \ell \\ \ell_1 & -\ell_1 & -m \end{pmatrix} = (-1)^{-\ell_1 + \ell_2 + m} \left[\frac{(2\ell_1)!(-\ell_1 + \ell_2 + \ell)!}{(\ell_1 + \ell_2 + \ell + 1)(\ell_1 - \ell_2 + \ell)!} \frac{(\ell_1 + \ell_2 + m)!(\ell - m)!}{(\ell_1 + \ell_2 - \ell)!(-\ell_1 + \ell_2 - m)!} \right]^{1/2}. \tag{33}$$

(A) *Modes with* $m = -1$.

We will consider the $m = -1$ term first:

$$\tilde{\Psi}^{\perp}_{\ell,m=-1}(k\hat{\mathbf{z}}; r) = -\sqrt{4\pi} \sqrt{\frac{2\pi}{3}} \tilde{\mathbf{q}}_{\perp}(k\hat{\mathbf{z}}; r) \sum_{\ell'} I_{\ell,\ell',1}\ j_{\ell'}(k\, r)\ \sqrt{\Sigma_{\ell'}} \begin{pmatrix} \ell' & \ell & +1 \\ 0 & 0 & 0 \end{pmatrix} \begin{pmatrix} \ell' & \ell & +1 \\ 0 & +1 & -1 \end{pmatrix}. \tag{34}$$

The 3j symbols get contribution from $\ell' = \ell + 1$ and $\ell' = \ell - 1$ due to the *triangular* inequality:

$$\tilde{\Psi}^{\perp}_{\ell,m=-1}(k\hat{\mathbf{z}}; r) = -\sqrt{4\pi} \sqrt{\frac{2\pi}{3}} \tilde{\boldsymbol{q}}_{\perp}(k\hat{\mathbf{z}}; r) \left[\sqrt{\Sigma_{\ell+1}} j_{\ell+1}(kr) I_{\ell,\ell+1,1} \begin{pmatrix} \ell+1 & \ell & +1 \\ 0 & 0 & 0 \end{pmatrix} \begin{pmatrix} \ell+1 & \ell & 1 \\ 0 & +1 & -1 \end{pmatrix} \right.$$
$$\left. + \sqrt{\Sigma_{\ell-1}} j_{\ell-1}(kr) I_{\ell,\ell-1,1} \begin{pmatrix} \ell-1 & \ell & +1 \\ 0 & 0 & 0 \end{pmatrix} \begin{pmatrix} \ell-1 & \ell & +1 \\ 0 & +1 & -1 \end{pmatrix} \right]. \tag{35}$$

We use the identities in equations (32) and (33) to derive the following expressions:

$$\begin{pmatrix} \ell+1 & \ell & +1 \\ 0 & 0 & 0 \end{pmatrix} = (-1)^{\ell+1} \sqrt{\frac{\ell+1}{\Sigma_\ell \Sigma_{\ell+1}}}; \quad \begin{pmatrix} \ell+1 & \ell & +1 \\ 0 & +1 & -1 \end{pmatrix} = (-1)^{\ell-1} \sqrt{\frac{\ell}{2\Sigma_\ell \Sigma_{\ell+1}}}. \tag{36}$$

We also use $I_{\ell,\ell\pm1,1} = \sqrt{3/4\pi}\sqrt{\Sigma_\ell}\sqrt{\Sigma_{\ell\pm1}}$ we eventually get:

$$\tilde{\Psi}^{\perp}_{\ell m=-1}(k\hat{\mathbf{z}}; r) = (-i)^{\ell+1}\ \sqrt{\pi \Pi_\ell \Sigma_\ell} \frac{j_\ell(kr)}{kr}\ \tilde{\mathbf{q}}_{\perp}(k\hat{\mathbf{z}}, r); \qquad \Pi_\ell \equiv \ell(\ell+1). \tag{37}$$

Where we have also used the following relation for the spherical Bessel functions:

$$j_{\ell+1}(x) + j_{\ell-1}(x) = \frac{\Sigma_\ell}{x} j_\ell(x). \tag{38}$$

(B) *Modes with* $m = +1$.

This component can also be computed in an analogous manner:

$$\tilde{\Psi}^{\perp}_{l,m=1}(k\hat{\mathbf{z}}; r) = \tilde{\mathbf{q}}_{\perp}(k\hat{\mathbf{z}}, r) \sum_{\ell'} I_{\ell\ell'1}\ j_{\ell'}(kr)\ \sqrt{\Sigma_{\ell'}} \begin{pmatrix} \ell' & \ell & +1 \\ 0 & 0 & 0 \end{pmatrix} \begin{pmatrix} \ell' & \ell & +1 \\ 0 & +1 & -1 \end{pmatrix}. \tag{39}$$

Following the same steps and using the following expressions for the 3*j* symbols:

$$\begin{pmatrix} \ell-1 & \ell & +1 \\ 0 & 0 & 0 \end{pmatrix} = (-1)^{\ell} \sqrt{\frac{\ell}{\Sigma_\ell \Sigma_{\ell-1}}}; \quad \begin{pmatrix} \ell-1 & \ell & +1 \\ 0 & +1 & -1 \end{pmatrix} = (-1)^{\ell-1} \sqrt{\frac{\ell+1}{2\Sigma_\ell \Sigma_{\ell-1}}}; \tag{40}$$

it can be shown that $\tilde{\Psi}^{\perp}_{\ell,m=1}(k\hat{\mathbf{z}}; r) = -\tilde{\Psi}^{\perp}_{\ell,m=-1}(k\hat{\mathbf{z}}; r)$.

(C) *Combining* $m = \pm 1$ *modes*.

Next, to rotate $\Theta^{\perp}_{\ell m'}(k\hat{\boldsymbol{z}})$ defined for k along the z-axis to an arbitrary observer's orientation $\Theta^{\perp}_{\ell m}(k)$, we use the expression $\tilde{\Psi}^{\perp}_{\ell m}(k) = \sum_{m'=\pm1} D^{\ell}_{mm'}(\hat{\Omega}_{\mathbf{k}}) \tilde{\Psi}^{\perp}_{\ell m'}(k\hat{\mathbf{z}})$, where D is the Wigner D-matrix, we can write equation (39) in following form:

$$\Theta^{\perp}_{\ell m}(k) = (-i)^{\ell+1}\ \sqrt{\pi \Pi_\ell \Sigma_\ell} \int \frac{d^3\boldsymbol{k}'}{(2\pi)^3} \sum_m D^{\ell}_{m,\pm1}(\hat{\boldsymbol{\Omega}}_{\mathbf{k}'}) \sqrt{\frac{2}{\pi}} \int dr\ \phi(r)\ k\ j_\ell(k\, r) \frac{j_\ell(k'r)}{k'r}\ \tilde{\mathbf{q}}_{\perp}(k'\hat{\mathbf{z}}; r). \tag{41}$$

(D) *Constructing the power spectra.*

Finally the 3D sFB covariance $\hat{\mathcal{C}}^{\perp}_{\ell}(k_1, k_2)$ can be expressed in terms of $P_{q\perp}$ as:

$$\hat{\mathcal{C}}^{\perp}_{\ell}(k_1, k_2) \equiv \langle \hat{\Theta}^{\perp}_{\ell m}(k_1) \hat{\Theta}^{*\perp}_{\ell m}(k_2) \rangle$$
$$= 2\Pi_\ell \int dk\ k^2 \int d\, r_1\ \phi(r_1)\ k_1 j_\ell(k_1 r_1) \frac{j_\ell(k\, r_1)}{kr_1} \int d\, r_2\ \phi(r_2)\ k_2\ j_\ell(k_2 r_2)\ \frac{j_\ell(k\, r_2)}{kr_2}\ P_{q\perp}(k; r_1, r_2). \tag{42}$$

To perform the $d\hat{\boldsymbol{\Omega}}_{\rm k}$ integral in equation (41) we use the following expression for the orthogonality of Wigner D-matrices:

$$\int d\hat{\boldsymbol{\Omega}}_{\rm k}\; D^{\ell}_{m_1,m_2}(\hat{\boldsymbol{\Omega}}_{\rm k})\; D^{\ell'}_{m'_1,m'_2}(\hat{\boldsymbol{\Omega}}_{\rm k}) = \frac{4\pi}{\Sigma_\ell}\delta^{\rm K}_{\ell\ell'}\delta^{\rm K}_{m_1m'_1}\delta^{\rm K}_{m_2m'_2}. \tag{43}$$

We note here that even for all-sky coverage the covariance matrix above can be ill-conditioned, reflecting the very nature of the kSZ effect which is inherently nonlinear even at linear regime due to coupling of modes resulting from density and velocity field. Thus a practical implementation may require binning to improve the condition number. The expression presented in equation (42) can be evaluated directly. In case of more conservative estimates one can directly evaluate using numerical simulations. Nevertheless we also quote results that use the following approximation $P_{q\perp}(k;r,r') \approx \sqrt{P_{q\perp}(k;r)}\sqrt{P_{q\perp}(k;r')}$ (Castro et al 2005) to reduce the dimensionality of the integration in equation (42).

$$\mathcal{C}^{\perp}_{\ell}(k_1,k_2) \approx \int\; k^2\; dk\; \mathcal{I}^{2\perp}_{\ell}(k,k_1)\; \mathcal{I}^{2\perp}_{\ell}(k,k_2); \tag{44}$$

$$\mathcal{I}^{2\perp}_{\ell}(k,k') \approx \sqrt{2\Pi_\ell}\int\; dr\; \phi(r)\; k\; j_\ell(kr)\; \frac{j_\ell(k'r)}{k'r}\; \sqrt{P_{q\perp}(k';r)}. \tag{45}$$

The kernel $\mathcal{I}^{\perp}_{\ell}(k,k')$ defined above encapsulates the information regarding the mode–mode coupling. Finally we recover the projected (2D) power spectrum for the kSZ effect is given by Ma & Fry (2002):

$$\mathcal{C}^{\perp}_{\ell} = \frac{1}{2}\int \frac{dr}{r^2}\; \phi^2(r)\; P_{q\perp}\left(k=\frac{\ell}{r};r\right). \tag{46}$$

The derivation of equation (46) depends on the use of Limber approximation stated below for an arbitrary function F:

$$\int\; k^2\; dk\; F(k) j_\ell(kr) j_\ell(kr') \approx \frac{\pi}{2r^2} F\left(k=\frac{\ell}{r}\right)\delta_D(r-r'); \tag{47}$$

which generalizes the orthogonality property of the spherical Bessel functions:

$$\int\; k^2\; dk\; j_\ell(kr) j_\ell(kr') = \frac{\pi}{2r^2}\delta_D(r-r'). \tag{48}$$

Cross-correlating the CMB maps $\Theta(\hat{\boldsymbol{\Omega}}) = \sum_{\ell m}\Theta_{\ell m}Y^*_{\ell m}(\hat{\Omega})$ against reconstructed 3D estimators:

$$\hat{\mathcal{C}}^{\perp}_{\ell}(k) \equiv \left\langle \Theta_{\ell m}\hat{\Theta}^{*\perp}_{\ell m}(k)\right\rangle = 2\Pi_\ell\; \int\; dk'\; k'^2\; \int d\, r_1\; r_1^2\; \phi(r_1)\; \frac{j_\ell(k'\, r_1)}{k' r_1}\int d\, r_2\; r_2^2\; \phi(r_2)\; k\; j_\ell(k\, r_2)\; \frac{j_\ell(k'\, r_2)}{k' r_2}\; P_{q\perp}(k';r_1,r_2). \tag{49}$$

Notice that the estimator $\hat{\boldsymbol{\Theta}}(\boldsymbol{r})$ is constructed using 3D distribution of galaxies and the recovered 3D velocity distribution. The weight $\phi(r)$ included in the construction depends on a prior choice of cosmology. The sFB expansion decomposes the reconstructed kSZ estimator to mode specified by $\{k\ell m\}$. The cross-correlation of this estimator with CMB maps $\Theta(\hat{\boldsymbol{\Omega}})$ thus extracts only kSZ contribution as a function of radial harmonics k and radial harmonics ℓ. This provides an unique method to recover radial information about evolution of kSZ effect. The construction has other advantages. It avoids any contamination from other CMB secondary anisotropies such as lensing or tSZ, or even from primary CMB and thus reduces the statistical error. Given that the kSZ signal is weak and foreground contamination (as well as confusion from dusty star-forming galaxies) is high at angular scales where kSZ peaks the method presented here offers an unique opportunity.

The estimator in equation (68) involves a 3D integral. We can use the same factorization of unequal time correlator introduced above to reduce its dimensionality:

$$\hat{\mathcal{C}}^{\perp}_{\ell}(k) \approx \int\; dk'\; k'^2\; \mathcal{I}^{2\perp}_{\ell}(k,k')\; \mathcal{I}^{\perp}_{\ell}(k'); \tag{50}$$

$$\mathcal{I}^{\perp}_{\ell}(k) \approx \int\; dr\, r^2\; \phi(r)\; \frac{j_\ell(kr)}{kr}\sqrt{P_{q\perp}(k;r)}. \tag{51}$$

Equation (49) and its simplified version equations (50) and (51) constitute some of the main results of this paper.

Few comments are in order. The primary aim of this paper is about separating the late-time kSZ, however the results presented here are in the sFB domain and the dependence on the radial coordinate remains implicit which is encoded in the function the function $\phi(r)$. Indeed it is also possible to rearrange equations (44) and (45) into equations (50) and (51), with r integrals appearing as outer integral. Mathematical relations relevant for projecting the 3D results on to redshift bins will be dealt with in Section 5.

(E) *Reconstructing the velocity field.*

The construction of the estimator introduced above for obtaining a 3D galaxy distribution from a 3D survey is just a first step. The galaxy density field $\delta_{\rm g}$ is used as a proxy for the underlying DM distribution δ. It is possible to incorporate redshift- and scale-dependent bias but at large scales where we will use our estimator, a simple linear bias $\delta_{\rm g} = b\delta$ should be sufficient. Construction of a kSZ estimator should include appropriate weighting using the recovered velocity field $\boldsymbol{v}$. This is required to avoid the cancellation of cross-correlation of density field and an estimator for kSZ due to the spinorial nature of the kSZ field. The reconstruction of 3D velocity field uses the linearized continuity equation as follows:

$$\dot{\delta} + \nabla\cdot\boldsymbol{v} = 0. \tag{52}$$

In Fourier space it takes the following form:

$$\hat{\boldsymbol{v}}(\boldsymbol{k}) = -if(z)H(z)\delta(\boldsymbol{k})\frac{\hat{\boldsymbol{k}}}{k}; \qquad f(z) \equiv \frac{d\ln D_+}{d\ln a}. \tag{53}$$

The estimator thus constructed using linear theory will be insensitive to multistreaming resulting from shell-crossing that introduces vorticity. However, nonlinearities at the perturbative level can be included in a more sophisticated treatment which we ignore here. The linear redshift-space distortion (the Kaiser effect) is ignored here but can be incorporated in our treatment (Munshi et al. 2015). A prior on background cosmology is required for specification of $H(z)$ and $f(z)$.

4.2 Evaluating the parallel components of the 3D sFB covariance $\mathcal{C}_\ell^\parallel(k, k')$ and the projected 2D power spectrum $\mathcal{C}_\ell^\parallel(k)$

The contribution from $\mathcal{C}_\ell^\parallel(k)$ can be used as a check on systematics. The computation of the *longitudinal* contribution or $\mathcal{C}_\ell^\parallel(k_1, k_2)$ in terms of $P_{q\parallel}$ follows similar steps

$$\Theta^\parallel(\boldsymbol{r}) = \phi(r)\int \frac{d^3\boldsymbol{k}'}{(2\pi)^3}\tilde{\Psi}^\parallel(\boldsymbol{k}', \boldsymbol{r}); \tag{54}$$

$$\tilde{\Psi}^\parallel(\boldsymbol{k};\boldsymbol{r}) = \cos\vartheta\ \tilde{\mathbf{q}}_\parallel(\boldsymbol{k};\boldsymbol{r})\mathrm{e}^{-\mathrm{i}\mathbf{k}\cdot\boldsymbol{r}}. \tag{55}$$

Using the fact:

$$\cos\vartheta = \sqrt{\frac{4\pi}{3}}\ Y_{1,0}(\hat{\boldsymbol{\Omega}}); \tag{56}$$

and taking advantage of Rayleigh expansion equation (26) we can write:

$$\tilde{\Psi}^\parallel(\boldsymbol{k};\boldsymbol{r}) = 4\pi\sqrt{\frac{4\pi}{3}}\ \tilde{\mathbf{q}}_\parallel(\boldsymbol{k}, r)\sum_{\ell m}(-1)^\ell j_\ell(kr)Y_{\ell m}(\hat{\boldsymbol{\Omega}})Y_{\ell m}(\hat{\boldsymbol{\Omega}}_{\rm k}). \tag{57}$$

Next, aligning the $\boldsymbol{k}$ vector along the z-axis ($\boldsymbol{k} = k\,\hat{\boldsymbol{z}}$) we use the identity $Y_{\ell m}(\hat{\boldsymbol{\Omega}}_{\rm k}) = \delta_{m0}\sqrt{\frac{\Sigma_\ell}{4\pi}}$:

$$\tilde{\Psi}^\parallel(k\hat{\boldsymbol{z}};\boldsymbol{r}) = 4\pi\sqrt{\frac{1}{3}}\ \tilde{\mathbf{q}}_\parallel(k\hat{\boldsymbol{z}}, r)Y_{10}(\hat{\Omega})\sum_{\ell'}\sqrt{\Sigma_{\ell'}}\,j_{\ell'}(kr)Y_{\ell'0}(\hat{\Omega}). \tag{58}$$

We perform a spherical harmonic transform of $\tilde{\Psi}^\parallel$. We note that the only non-zero harmonic coefficients come from $\underline{m = 0}$. Using the expression $I_{\ell,\ell\pm1,1} = \sqrt{3/4\pi}\sqrt{\Sigma_\ell}\sqrt{\Sigma_{\ell\pm1}}$

$$\tilde{\Psi}^\parallel_{\ell,m=0}(k\hat{\boldsymbol{z}}) = 4\pi\sqrt{\frac{1}{3}}\ \tilde{\mathbf{q}}_\parallel(k\hat{\boldsymbol{z}};r)\sum_{\ell'}(-i)^{\ell'}I_{\ell\ell'1}\ j_{\ell'}(kr)\sqrt{\Sigma_{\ell'}}\begin{pmatrix}\ell' & \ell & +1\\ 0 & 0 & 0\end{pmatrix}^2. \tag{59}$$

As before, due to the triangular inequality, only terms that contribute are $\ell' = \ell \pm 1$

$$\tilde{\Psi}^\parallel_{\ell,m=0}(k\hat{\boldsymbol{z}};r) = 4\pi\sqrt{\frac{1}{3}}\tilde{\mathbf{q}}_\parallel(k\hat{\boldsymbol{z}};r)\Bigg[(-i)^{\ell+1}I_{\ell,\ell+1,1}j_{\ell+1}(kr)\sqrt{\Sigma_{\ell+1}}\begin{pmatrix}\ell+1 & \ell & +1\\ 0 & 0 & 0\end{pmatrix}^2$$
$$+(-i)^{\ell-1}I_{\ell,\ell-1,1}j_{\ell-1}(kr)\sqrt{\Sigma_{\ell-1}}\begin{pmatrix}\ell-1 & \ell & +1\\ 0 & 0 & 0\end{pmatrix}^2\Bigg]. \tag{60}$$

Using the expression in equations (36) and (40) for the 3j symbols that appear in the above expression we can write:

$$\tilde{\Psi}^\parallel_{\ell,m=0}(k\hat{\boldsymbol{z}};r) = -(-i)^{\ell+1}\sqrt{\frac{4\pi}{\Sigma_\ell}}\tilde{\mathbf{q}}_\parallel(k\hat{\boldsymbol{z}};r)\left[(\ell+1)j_{\ell+1}(kr) - \ell\, j_{\ell-1}(kr)\right]. \tag{61}$$

Next we use the following recurrence relation for $j_\ell(x)$ to simplify further:

$$\ell\, j_{\ell-1}(x) - (\ell+1)j_{\ell+1}(x) = \Sigma_\ell\ j'_\ell(k\,r). \tag{62}$$

Here the prime denotes a derivative w.r.t. the argument. Using this expression we can write:

$$\tilde{\Psi}^\parallel_{\ell,m=0}(k\hat{\boldsymbol{z}}) = \sqrt{4\pi\Sigma_\ell}\ \tilde{\mathbf{q}}_\parallel(k\hat{\boldsymbol{z}};r)\ j'_\ell(kr). \tag{63}$$

For higher ℓ the contribution from $j_{\ell-1}$ and $j_{\ell+1}$ nearly cancels each other thus making $\mathcal{C}_\ell^\parallel(k)$ sub dominant. Performing the rotation using Wigner $D^\ell_{mm'}$- matrices as before to a general orientation we have:

$$\tilde{\Psi}^\parallel_{\ell m}(k) = (-i)^{\ell+1}\ \sqrt{4\pi\Sigma_\ell}\ \int\frac{d^3\boldsymbol{k}'}{(2\pi)^3}\sum_m D^\ell_{m,0}(\hat{\boldsymbol{\Omega}}_{k'})\int dr\ r^2\ \phi(r)\ k\ j_\ell(k\,r)\ j'_\ell(k'\,r)\ \tilde{\mathbf{q}}_\parallel(k'\hat{\boldsymbol{z}}, r). \tag{64}$$

Finally using the orthogonality relation for Wigner D-matrices given in equation (43), and the definition $P_{q\parallel}$ in equation (18) we arrive at the following expression:

$$\mathcal{C}_\ell^{\parallel}(k_1,k_2) \equiv \langle \hat{\Theta}^{\parallel}_{\ell m}(k_1)\hat{\Theta}^{*\parallel}_{\ell m}(k_2)\rangle$$
$$= 2\Pi_\ell \int dk\, k^2 \int d\,r_1\, r^2\, \phi(r_1)\, k_1\, j_\ell(k_1 r_1) j'_\ell(k\, r_1) \int d\,r_2\, r^2\, \phi(r_2)\, k_2\, j_\ell(k_2 r_2)\, j'_\ell(k\, r_2)\, P_{q\parallel}(k; r_1, r_2). \quad (65)$$

Consequently, we can use the approximation $P_{q\parallel}(k;\, r, r') \approx \sqrt{P_{q\parallel}(k;\, r)}\sqrt{P_{q\parallel}(k;\, r')}$ to factorize the integrals:

$$\mathcal{C}_\ell^{\parallel}(k_1,k_2) \approx \int k^2\, dk\, \mathcal{I}_\ell^{2\parallel}(k,k_1)\, \mathcal{I}_\ell^{2\parallel}(k,k_2); \quad (66)$$

$$\mathcal{I}_\ell^{2\parallel}(k,k') \approx \sqrt{\frac{2}{\pi}} \int dr\, r^2\, \phi(r)\, k\, j_\ell(kr)\, r^2\, j'_\ell(k'\, r)\, \sqrt{P_{q\parallel}(k;r)}. \quad (67)$$

Cross-correlating the 2D CMB maps against reconstructed 3D estimators:

$$\hat{\mathcal{C}}_\ell^{\parallel}(k) \equiv \left\langle \Theta_{\ell m} \hat{\Theta}^{*\parallel}_{\ell m}(k) \right\rangle = 2\Pi_\ell \int dk'\, k'^2 \int d\,r_1\, r_1^2 \phi(r_1)\, j'_\ell(k'\, r_1) \int d\,r_2\, r_2^2\, \phi(r_2)\, k\, j_\ell(k\, r_2)\, j'_\ell(k'\, r_2)\, P_{q\parallel}(k'; r_1, r_2). \quad (68)$$

The corresponding expressions using the factorization are as follows:

$$\hat{\mathcal{C}}_\ell^{\parallel}(k) \approx \int dk'\, k'^2\, \mathcal{I}_\ell^{2\parallel}(k,k')\, \mathcal{I}_\ell^{\parallel}(k'); \quad (69)$$

$$\mathcal{I}_\ell^{\parallel}(k) \approx \sqrt{\frac{2}{\pi}} \int dr\, r^2\, \phi(r)\, j'_\ell(kr) \sqrt{P_{q\parallel}(k;r)}. \quad (70)$$

Various approximations are typically used to collapse a full 3D analysis to projection (2D) or, in other words to perform tomography (see Section 5). However, these methods invariably involve binning in redshift interval with a consequent loss of the information content of the data. The 3D analysis also gives the freedom to treat the angular and radial modes separately. Projection is achieved using Limber approximation invariably links the radial and angular modes. In projected or tomographic survey it is very difficult to disentangle individual scales. Treatment of individual scales independently is important for keeping a handle on the effect of nonlinearity due to gravitational evolution. A 3D analysis treats each galaxy individually and thus can be used to control the systematics at a level of individual galaxies, which is very important for kSZ reconstruction. Any contaminating region can always be masked out. A pseudo-$\mathcal{C}_\ell$ (PCL) based approach will be developed that can be used to recover the power spectra in the presence of mask (see Appendix).

5 PROJECTING 3D ON TO TOMOGRAPHY AND 2D

In order to connect with the tomographic reconstruction of kSZ effect by (Shao et al. 2011a), in this section we will show how to reconstruct the tomographic power spectra from the 3D power spectra we have developed. The tomographic estimator $\hat{\mathbf{\Theta}}^{\perp(i)}$ from the ith bin as introduced in equation (21) and its harmonic coefficients $\Theta^{\perp(i)}_{\ell m}$ can be expressed in terms of their 3D counterparts :

$$\hat{\mathbf{\Theta}}^{\perp(i)} = \int_{r_i}^{r_{i+1}} dr\, w(r)\, \hat{\Theta}^{\perp}(\boldsymbol{r}); \quad (71)$$

$$\hat{\mathbf{\Theta}}^{\perp(i)}_{\ell m} = \int d\hat{\mathbf{\Omega}}\, Y_{\ell m}(\hat{\mathbf{\Omega}}) \sqrt{\frac{2}{\pi}} \sum_{\ell' m'} \int dk\, k\, j_\ell(kr)\, Y_{\ell' m'}(\hat{\mathbf{\Omega}})\, \Theta^{\perp}_{\ell' m'}(k). \quad (72)$$

Using the orthogonality property of spherical harmonics we can express the $\Theta^{\perp(i)}_{\ell m}$ in terms of $\Theta^{\perp}_{\ell m}(k)$ using a kernel $T^{(i)}_\ell(k)$. The ith bin is defined between the radial distance r_i and r_{i+1}.

$$\hat{\mathbf{\Theta}}^{\perp(i)}_{\ell m} = \int dk\, \mathcal{J}^{(i)}_\ell(k) \hat{\mathbf{\Theta}}^{\perp}_{\ell m}(k); \qquad T^{(i)}_\ell(k) = \sqrt{\frac{2}{\pi}} k \int_{r_i}^{r_{i+1}} dr\, j_\ell(k\, r)\, w(r). \quad (73)$$

The tomographic power spectra for the ith bin is denoted as $\mathcal{C}^{\perp(i)}_\ell$. Similarly the covariance between ith and jth bin is denoted as $\mathcal{C}^{\perp(ij)}_\ell$

$$\hat{\mathcal{C}}^{\perp(ij)}_\ell \equiv \left\langle \hat{\Theta}^{\perp(i)}_{\ell m} \hat{\Theta}^{\perp(j)*}_{\ell m} \right\rangle = \int dk\, \mathcal{J}^{(i)}_\ell(k) \int dk'\, \mathcal{J}^{(j)}_\ell(k')\, \mathcal{C}^{\perp}_\ell(k,k'); \quad (74)$$

$$\hat{\mathcal{C}}^{\perp(i)}_\ell \equiv \left\langle \hat{\Theta}^{\perp(i)}_{\ell m} \Theta^{*}_{\ell m} \right\rangle = \int dk\, \mathcal{J}^{(i)}_\ell(k) \mathcal{C}^{\perp}_\ell(k). \quad (75)$$

Similar expressions were derived by ? in the context of 3D weak lensing. An exactly similar relation can be obtained for $\mathcal{C}^{\parallel(ij)}_\ell$ and $\mathcal{C}^{\parallel(i)}_\ell$. To construct the 2D estimator given in equation (46) we need to use only one bin and use the Limber approximation with $w = 1$.

The tomography essentially probes discrete sets of physical wave numbers. The position of the tomographic bins constraints the radial wave numbers probed as a function of angular harmonics. The advantage of 3D is being able to ensure the integrated analysis of the entire

set of wave-numbers probed by a survey. Indeed, tomography allows for straightforward interpretation of the results particularly redshift dependence of the kSZ signal. However, using Limber approximation as outlined above can always be used to collapse the 3D information to tomographic bins.

6 SIGNAL-TO-NOISE RATIO OF RECONSTRUCTION

A simplistic expression for the signal-to-noise ratio (S/N) for reconstruction of the individual modes described by radial and angular wave numbers (k, ℓ) respectively is given by:

$$\left(\frac{S}{N}\right)^{\perp}_{\ell}(k) = f_{\rm sky}\sqrt{\frac{2\ell+1}{2}}\frac{\mathcal{C}^{\perp}_{\ell}(k)}{\sqrt{\mathcal{C}^{\perp}_{\ell}(k,k)\mathcal{C}^{\rm CMB}_{\ell}+\mathcal{C}^{\perp}_{\ell}(k)\mathcal{C}^{\perp}_{\ell}(k)}}. \tag{76}$$

Expressions for $\mathcal{C}^{\perp}_{\ell}(k,k')$ is derived in equation (44) and $\mathcal{C}^{\perp}_{\ell}(k)$ in equation (51). We have ignored the off-diagonal terms of the covariance matrix in equation (76). For lower order multipoles $\ell < 100$, including the off-diagonals can make the covariance matrix singular. For all-sky coverage binning the matrix in few k bins (<5) improves the conditionality of the covariance matrix. The CMB power spectrum $\mathcal{C}^{\rm CMB}_{\ell}$ should also include the tSZ power spectrum at high-ℓ for (S/N) estimation. We assume the noise of estimation to be independent of CMB noise; $f_{\rm sky}$ denotes the fraction of sky covered. A similar expression for $\mathcal{C}^{\parallel}_{\ell}(k)$ can be obtained by replacing $\mathcal{C}^{\perp}_{\ell}(k)$ and $\mathcal{C}^{\perp}_{\ell}(k)$ with $\mathcal{C}^{\parallel}_{\ell}(k)$ and $\mathcal{C}^{\parallel}_{\ell}(k)$.

7 INPUT POWER SPECTRA FOR $\tilde{\mathbf{q}}_{\parallel}$ AND $\tilde{\mathbf{q}}_{\perp}$

The computation of the kSZ power spectra depends on modelling $P_{q\perp}$. Early analytical results were based on the linear perturbation theory and ignored nonlinearity in density and velocity field (Vishniac 1987). The kSZ effect in linear regime is also known as the Ostriker–Vishniac effect (Ostriker & Vishniac 1986). In Hu (2000) the linear theory prediction for the density power spectrum was replaced with nonlinear prescription for density power spectrum by Peacock & Dods (1996). The velocity power spectrum was from linear theory prediction [see e.g. Dodelson & Jubas (1993) and Hu (2000) for a detailed discussion of this issue]. In Ma & Fry (2002) the nonlinear power spectrum used was that from halo-model prescription. We outline the major step in the derivation to underline the approximations used in various steps. In terms of density $\tilde{\delta}(\boldsymbol{k})$ and velocity $\boldsymbol{v}(k)$ components we have:

$$\tilde{\mathbf{q}}_{\parallel}(\boldsymbol{k}) = \int \frac{d^3\boldsymbol{k}'}{(2\pi)^3}\,\mu\,\hat{\mathbf{\Omega}}_k\;\tilde{\mathbf{v}}(k')\tilde{\delta}(|\boldsymbol{k}-k'|); \tag{77}$$

$$\tilde{\mathbf{q}}_{\perp}(\boldsymbol{k}) = \int \frac{d^3\boldsymbol{k}'}{(2\pi)^3}(\hat{\mathbf{\Omega}}_{k'}-\mu\hat{\mathbf{\Omega}}_k)\tilde{\mathbf{v}}(k')\tilde{\delta}(|\boldsymbol{k}-k'|); \quad \mu = \hat{\mathbf{\Omega}}\cdot\hat{\mathbf{\Omega}}_{\rm k}. \tag{78}$$

The corresponding 3D power spectra are given by:

$$P_{q\perp}(k,r) \equiv \langle\tilde{\mathbf{q}}_{\perp}(\boldsymbol{k})\tilde{\mathbf{q}}^{*}_{\perp}(\boldsymbol{k})\rangle = \int \frac{d^3\boldsymbol{k}'}{(2\pi)^3}\left[(1-\mu'^2)P_{\delta\delta}(|\boldsymbol{k}-k'|)P_{vv}(k') - \frac{(1-\mu'^2)k'}{|\boldsymbol{k}-k'|}P_{\delta v}(|\boldsymbol{k}-k'|)P_{\delta v}(k')\right]; \tag{79}$$

$$P_{q\parallel}(k,r) \equiv \langle\tilde{\mathbf{q}}_{\parallel}(\boldsymbol{k})\tilde{\mathbf{q}}^{*}_{\parallel}(\boldsymbol{k})\rangle = \int \frac{d^3\boldsymbol{k}'}{(2\pi)^3}\left[\mu'^2 P_{\delta\delta}(|\boldsymbol{k}-k'|)P_{vv}(k') + \frac{(k-k'\mu')\mu'}{|\boldsymbol{k}-k'|}P_{\delta v}(|\boldsymbol{k}-k'|)P_{\delta v}(k')\right]. \tag{80}$$

These expressions were computed by neglecting the connected fourth-order moments which were found to be negligible. We will use the following expression from Vishniac (1987) [see also Jaffe & Kamionkowski (1998); Ma & Fry (2002); Park et al. (2016)] in our derivation of the 3D kSZ power spectrum:

$$P_{q\perp}(k,r) = \dot{a}^2 f^2 \int \frac{d^3\boldsymbol{k}'}{(2\pi)}P_{\delta\delta}(|k-k'|)P_{\delta\delta}(k')\frac{k(k-2k'\mu)(1-\mu'^2)}{k'^2(k^2+k'^2-2kk'\mu')}. \tag{81}$$

$$P_{q\parallel}(k,r) = \dot{a}^2 f^2 \int \frac{d^3\boldsymbol{k}'}{(2\pi)}P_{\delta\delta}(|k-k'|)P_{\delta\delta}(k')\frac{k\mu'(k\mu'-2k'\mu'^2+k')}{k'^2(k^2+k'^2-2kk'\mu')}; \qquad f \equiv \frac{d\ln D_+}{d\ln a}. \tag{82}$$

The above expressions were derived under the assumption $P_{\delta\theta}(|k-k'|)P_{\delta\theta}(k') = P_{\delta\delta}(|k-k'|)P_{\theta\theta}(k')$ [see e.g. Ma & Fry (2000), and references therein]. This approximation is a necessary ingredient as the density–velocity cross-correlation is poorly understood. In the linear theory the velocity and cross-correlation power spectra are expressed as follows:

$$P_{vv}(k) = \left(\frac{f\dot{a}}{k}\right)^2 P_{\delta\delta}(k); \qquad P_{\delta v}(k) = \left(\frac{f\dot{a}}{k}\right)P_{\delta\delta}(k). \tag{83}$$

To evaluate the kSZ power spectra defined in equation (50) and equation (70) we use these expressions for $P_{q\perp}(k,r)$ and $P_{q\parallel}(k,r)$. Following Ma & Fry (2000) we use the halo model to compute the density power spectra and linear theory to compute the velocity power spectrum [see Dodelson & Jubas (1993) and Hu (2000) for related discussions]. In the high -k limit equations (79) and (80) are approximated as:

$$P_{q\perp}(k) = \frac{2}{3}P_{\delta\delta}(k)\;v^2_{\rm rms}(k); \qquad P_{q\perp}(k) = 2P_{q\parallel}(k); \qquad v^2_{\rm rms}(k) \equiv \int_{k'\le k}\frac{d^3k'}{(2\pi)^3}P_{vv}(k'). \tag{84}$$

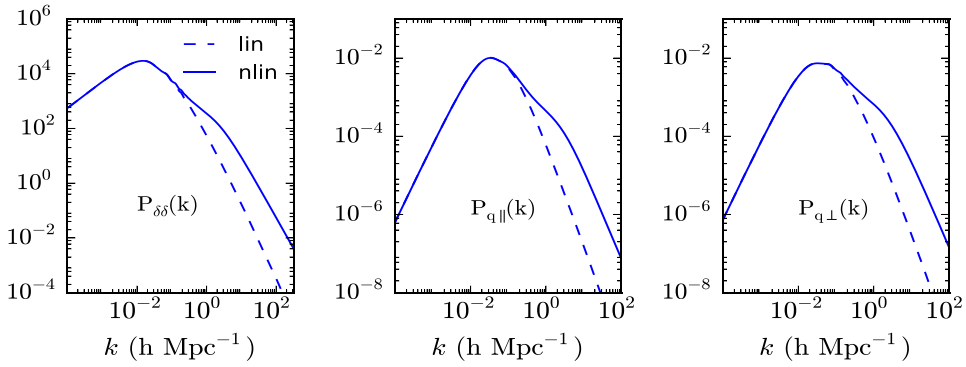

Figure 1. The power spectrum $P_{q\parallel}(k)$ for $\boldsymbol{q}_\parallel$ (middle panel) and $P_{q\perp}(k)$ (right-hand panel) for $\boldsymbol{q}_\perp$ defined in equation (18) are plotted along with the matter power spectrum $P_{\delta\delta}(k)$ in the left-hand panel as a function of k (hMpc^{-1}). The dashed (solid) lines represent results obtained using linear (nonlinear) results. The results are shown for $z = 0$.

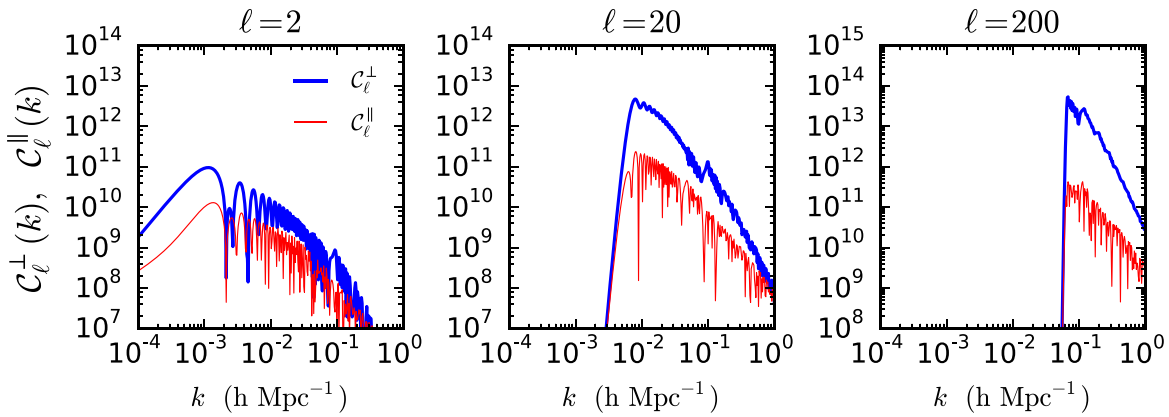

Figure 2. The power spectra $\mathcal{C}_\ell^\perp(k)$ [defined in equation (50)] and $\mathcal{C}_\ell^\parallel(k)$ [defined in equation (70)] are displayed for $\ell = 2$ (left-hand panel), $\ell = 20$ (middle-panel) and $\ell = 200$ (right-hand panel). The reconstruction was extended up to a maximum rdshift of $z = 1$. The power spectra are computed using underlying nonlinear matter power spectra.

Here $v_{\rm rms}^2$ is the velocity dispersion. In a recent study the effect of the four-point correlation function, which we have ignored in our study has been outlined by Park et al. (2016). They pointed out that in the nonlinear regime at $k > 0.1h$Mpc^{-1} the contribution from the four-point correlation function (connected-part) can reach as high as 10 per cent.

8 RESULTS AND DISCUSSION

In Fig. 1 we show the input power spectra $P_q(k, z)$ (right-hand panel), $P_{q\perp}(k, z)$ (left-hand panel), and $P_{q\parallel}(k, z)$ (middle-panel) used for our calculation. The solid lines represent nonlinear power spectra and the dashed lines linear power spectra. The results are for $z = 0$. In general, to relate the baryonic power spectrum and the DM power spectrum a window function is used. We have not included any such filtering in our computation to keep the analysis transparent, however such modification is straightforward. Notice that the treatment we followed involves using the linear relationship in equation (53) between density and velocity, which breaks down at high k. Accurate modelling in that regime can only be obtained using numerical simulations. Nevertheless, we believe that the qualitative nature of our results will remain unchanged in the range of (k, ℓ) considered here. The approximate form of the power spectrum we have chosen that allows us to separate two internal integrals and reduces computation time significantly. Indeed it can be argued that presence of spherical Bessel functions introduces a cut-off that suppresses long range (low-ℓ) modes thus justifying such a factorization.

In Fig. 2 we show the computed $\mathcal{C}_\ell^\perp(k)$ and $\mathcal{C}_\ell^\parallel(k)$ as a function of k for $\ell = 2$, 20, and 200. These spectra were defined in equation (44) and equation (50), respectively. The spectra correspond to a maximum redshift of reconstruction of $z = 1$. Different panels correspond to harmonics $\ell = 2$, 20 and 200 from left to right. The peak of the spectra shifts to higher k with increasing ℓ. Due to the presence of the spherical Bessel functions, which become increasingly sharp-peaked, the 3D cross-spectra effectively collapse to the projected ones at higher ℓs, thus virtually linking the radial wavenumber k and the angular wavenumber ℓ. The range of k that contributes to a given ℓ becomes more sharply defined.

The power spectrum $\mathcal{C}_\ell^\perp(k)$ increasingly dominates over $\mathcal{C}_\ell^\parallel(k)$ with increasing ℓ. In Fig. 3 the diagonal entries for 3D covariance $\mathcal{C}_\ell^\perp(k, k)$ (solid-curves) and $\mathcal{C}_\ell^\parallel(k, k)$ (dashed-curves) are shown as a function of wavenumber $k(h^{-1}$ Mpc). These covariances are defined in equation (44) and equation (66), respectively. These plots show diagonal cuts in the (k, k') plane for various ℓ values through the 3D covariance

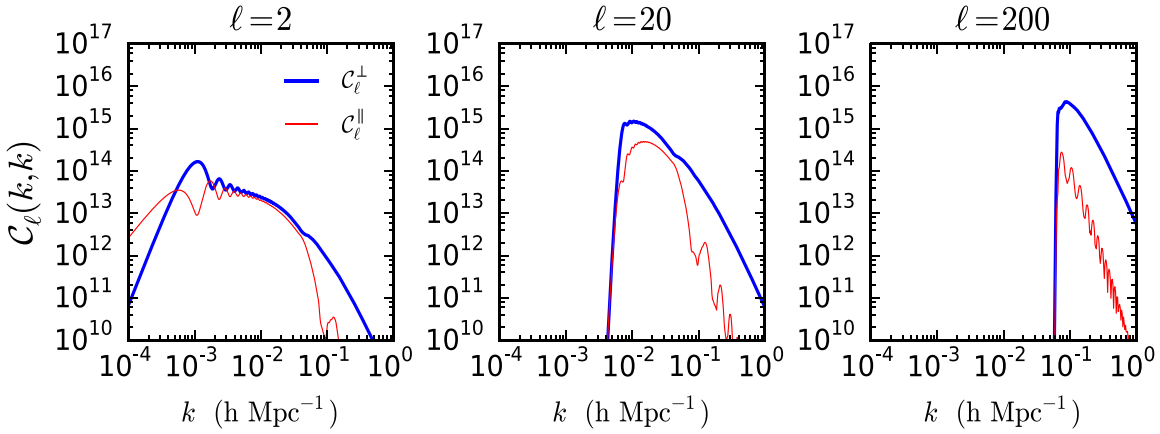

Figure 3. The diagonal components of the 3D covariance matrix $\mathcal{C}_\ell^\perp(k, k')$ [defined in equation (44)] and $\mathcal{C}_\ell^\parallel(k, k')$ [defined in equation (65)] are displayed for $\ell = 2$ (left-hand panel), $\ell = 20$ (middle-panel) and $\ell = 200$ (right-hand panel). The reconstruction was extended up to a maximum rdshift of $z = 1$. The power spectra are computed using underlying nonlinear matter power spectra.

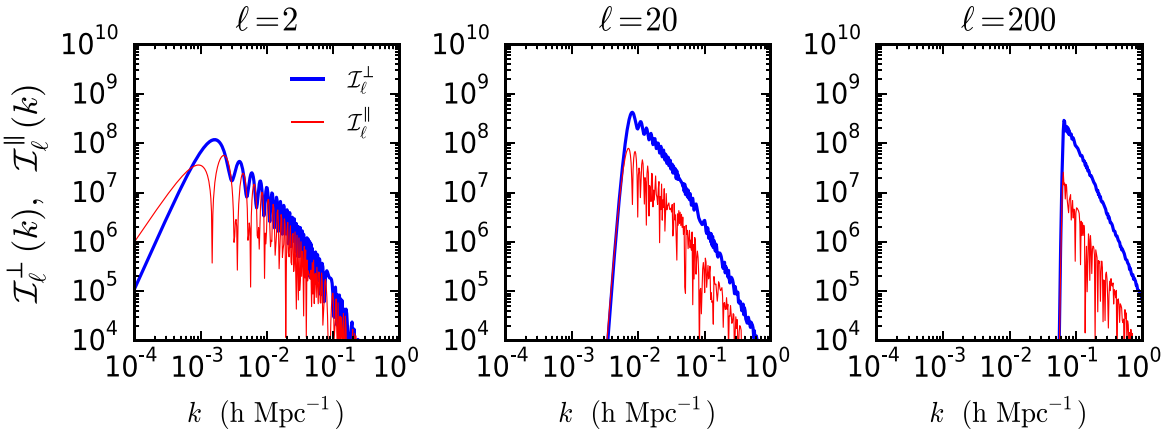

Figure 4. The diagonal entries of the 2D kernels $\mathcal{I}_\ell^\perp(k)$ and $\mathcal{I}_\ell^\parallel(k)$ defined in equation (51) and equation (70) are plotted as a function of the wavenumber k in hMpc^{-1}. The panels from left to right correspond to $\ell = 2$, 20 and 200, respectively. Reconstruction is performed up to a maximum redshift of $z = 1$. Underlying matter power spectrum is assumed to be nonlinear.

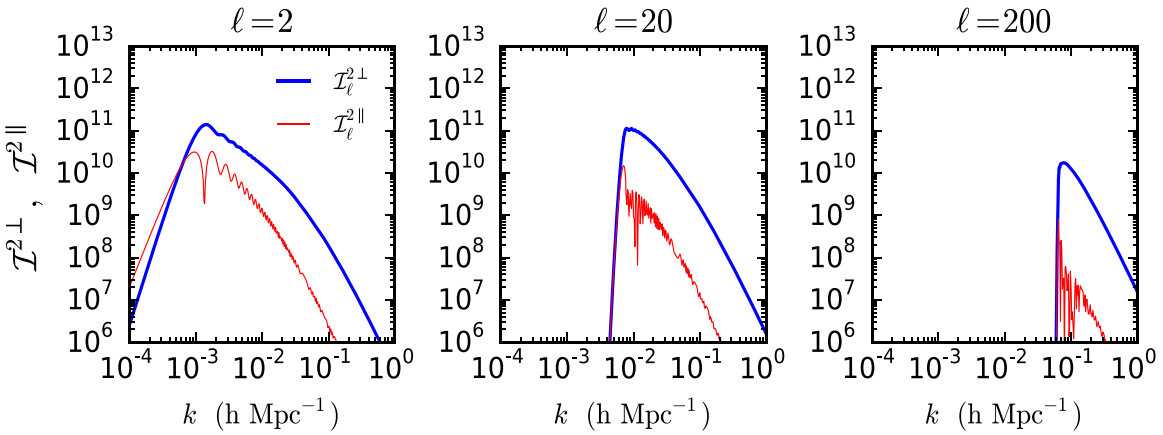

Figure 5. The diagonal entries of the kernels $\mathcal{I}_\ell^{2\perp}(k, k')$ and $\mathcal{I}_\ell^{2\parallel}(k, k')$ defined in equation (45) and equation (67) are plotted as a function of the wavenumber k in h^{-1} Mpc.

matrices. The effect of the Bessel function is to introduce a sharp cut-off on the long wavelength contributions with $k < \ell/r_{\rm max}$, where $r_{\rm max}$ is the extent of the survey. As the ℓ values increases the diagonal entries terms of the covariance do not become significant until $kr_{\rm max} \approx \ell$.

The kernels $\mathcal{I}_\ell^\perp(k)$ and $\mathcal{I}_\ell^\parallel(k)$ which are used to construct the cross-spectra $\mathcal{C}_\ell^\parallel(k)$ (dashed-lines) and $\mathcal{C}_\ell^\perp(k)$ (solid-lines) as a function of wavelength are plotted in Fig. 4. The corresponding kernels $\mathcal{I}_\ell^{2\perp}(k, k')$ and $\mathcal{I}_\ell^{2\parallel}(k, k')$ are shown in Fig. 5.

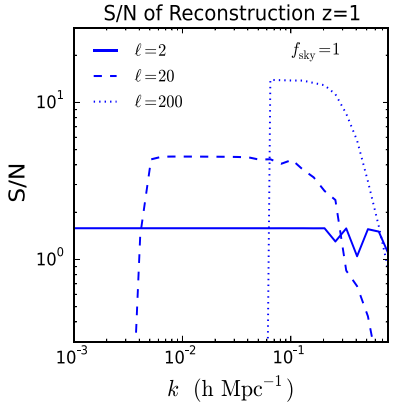

Figure 6. We show an order of magnitude estimate of the signal-to-noise ratio introduced in equation (76) for three modes with angular harmonics represented by $\ell = 2$, 20 and 200 as a function of their radial wavenumber $k(h^{-1}$ Mpc) (see the text for more details). We assume an all-sky coverage $f_{\rm sky} = 1$.

In Fig. 6 we display the result of (S/N) computed using equation (76). We show results for $\ell = 2$, 20 and 200 as a function of the radial wavenumber k. The reconstruction is assumed to be done up to a redshift of $z = 1$. We ignore the residuals from component separation. We also ignore the shot-noise due to finite number density of galaxies. However, the S/N of maps from galaxy surveys are much higher compared to their CMB counterpart and are not likely affect the S/N of the reconstruction. Higher multipoles have better (S/N) of reconstruction primarily due to the $2\ell + 1$ prefactor. However, the available range of radial wavenumber k decreases with increasing ℓ. At higher k the linear reconstruction of velocity from density field may not be accurate. Increasing the survey depth will clearly shift the peak of the reconstructed $\mathcal{C}_\ell(k)$ to lower radial wave-numbers k, but, number density of galxies used for reconstruction will decrease thus decreasing the S/N. Maps from future 21 cm surveys or other tracers of large-scale structure can be used to extend the reconstruction technique proposed here to moderate redshifts $z < 3$.

9 CONCLUSIONS AND OUTLOOK

The kSZ signal is overwhelmed by various contaminations and lacks any redshift information due to the projection effect. Moreover, the contribution to kSZ can be from the reionization epoch as well as from post-reionization era. The contribution from reionization depends on accurate modelling of reionization which can in principle be inhomogeneous (patchy) and thus difficult to model. With the recent detection of kSZ effect there is a greater effort in the community to understand it than was previously. In this paper we focus on estimation of post-reionization late-time kSZ effect. This contribution is relatively easier to model as the physics involve is simpler compared to reionization and may provide us clues about our local universe and when subtracted from the total kSZ can help constrain the contribution originating from reionization.

Indeed from CMB measurements alone, we only expect to detect kSZ from the auto power spectra of temperature fluctuations. However, kSZ is likely to dominate the power spectrum at $\ell > 3000$ where the primary CMB is damped due to silk-damping and contribution from tSZ shows a null at $\nu = 217$ GHz. The method proposed here can probe kSZ below $\ell < 3000$ as the method proposed here is independent of contamination from primary CMB or other secondary anisotropies.

The method proposed here uses spectroscopic galaxy surveys to reconstruct peculiar velocity field. Our method weighs the peculiar velocity field with galaxy distribution. The resulting momentum when projected along the LoS direction can act as an estimator for kSZ effect in 3D. Our analysis extends previous analysis performed using tomographic bins (Ho et al. 2009; Shao et al. 2011a) and allows maximal exploitation of the available data with greater degree of freedom. We have constructed two different 3D estimators for kSZ power spectrum $\mathcal{C}_\ell^\perp(k)$ in equation (67) and $\mathcal{C}_\ell^\parallel(k)$ in equation (45) that can be used to extract information. This will eliminate any contamination from primary CMB which remains one of the dominant source especially at low ℓ. The tSZ contribution to CMB sky is typically removed by using frequency information. The lensing of CMB and kSZ lacks any frequency information. In the past, several methods have been proposed to separate such contribution, including the use of higher-order information or the non-Gaussianity of the signal. Most of the CMB secondary anisotropies originate in the relatively low-redshift universe and have a characteristic redshift evolution. Using this fact we propose a cross-correlation based estimator to extract kSZ effect from CMB maps. The proposal is based on using the spectroscopic redshift surveys to construct an estimator for the peculiar velocity and density. With suitable weighting these reconstructed fields can next be used to construct an estimator for kSZ that takes into account the spin-1 nature of kSZ. When cross-correlated with the CMB sky it will only cross-correlate with the kSZ component thus avoiding usual contamination from other secondaries. There are many advantages to the technique developed here. It separates the late time, $(0 < z < 3)$ contribution to kSZ effect from the poorly understood *patchy reionization* scenarios.

The kSZ effect is known to be a potentially powerful probe of the baryons – the estimators presented here can exploit this to probe directly the 3D distribution of the missing baryons in the low-redshift universe. The galaxy surveys typically have relatively higher (S/N) and are thus expected to allow such reconstruction. For tomographic reconstruction using Planck as target CMB survey and BOSS as a spectroscopic galaxy survey a (S/N) of 50 was shown to be achievable. It is expected that SZ survey e.g. SPT and galaxy surveys such as ADEPT, Euclid

and SKA would work still better. This will thus provide measurement of the power spectra over a range of scales (ℓ and k) with a reasonable accuracy. The detection of baryons using the methods presented here using kSZ signature in CMB maps does not rely on detection of hot gas or metals; it directly detects the free electrons in the IGM. The LoS velocity is uncorrelated with many standard systematics that plague usual power-spectrum analysis applied to CMB data, e.g. it is insensitive to the unsubtracted tSZ, galactic foregrounds and detector noise. We have ignored the redshift space distortion in our formulation of an estimator for the kSZ. The redshift space distortion can be effectively accounted for in the our 3D formulation at least at scales where linear Kaiser effect remains valid. At smaller scales higher order contributions will have to be included. However at even smaller scales the finger-of-god effect caused by small scale random motion becomes important especially at low redshift where the perturbative results break down. Indeed our modelling of galaxy bias which we take as a linear and deterministic can also be stochastic [see e.g. Ahn et al. (2015), and references therein]. Such issues can only be dealt with through full numerical simulations.

The 3D reconstruction technique developed here is more fundamental than the tomographic methods presented previously. Indeed the tomographic or the projected power spectra can both be constructed from the 3D power spectra presented here. The 3D sFB transforms developed here generalizes similar expansion schemes used in other areas in cosmology including e.g. studies of weak lensing (Castro et al 2005) and redshift space distortions (Pratten & Munshi 2013).

We have already emphasized the power of kSZ to map out the baryonic web. Constraints on the dark sector, i.e. decaying DM or DM–DE interactions has recently attracted a lot of attention. They can be probed by tSZ or kSZ effects (e.g. Xu et al. 2013). The power spectra $P_{q\perp}$ and $P_{q\parallel}$ depend on the underlying matter power spectra $P_\delta(k)$ as well as on the growth rate of perturbations, f, see equations (81) and (82). Clearly in many modified gravity theories such as the $f(R)$ theories, the Dilaton theories and the K-mouflage models the power spectrum as well as the function $f(z)$ are very different from their ΛCDM counterparts. Future surveys with accurate determination of the kSZ power spectrum may be able to constrain such theories. Such issues in the context of 3D kSZ that we have studied here will be presented elsewhere.

ACKNOWLEDGEMENTS

DM, ITI, KLD and PC acknowledge support from the Science and Technology Facilities Council (grant number ST/L000652/1). The power spectrum $P_{q\perp}(k)$ and $P_{q\parallel}(k)$ used in this work was computed by G. W. Pettinari. We acknowledge useful discussion with H. Park and P. Zhang. DM also acknowledges results obtained by G. Pratten at the early stage of this work which helped obtaining some of the results presented here. DM benefited from discussions with A. Heavens and P. Valageas.

REFERENCES

Ahn K., Iliev I. T., Shapiro P. R., Srisawat C., 2015, MNRAS, 450, 1486
Atrio-Barandela F., Mucket J. P., Génova-Santos R., 2008, ApJ, 674, L61
Ayaita Y., Schaefer B. M., Weber M., 2012, MNRAS, 422, 3056
Ballinger W. E., Heavens A. F., Taylor A. N., 1995, MNRAS, 276, L59
Battaglia N., Natarajan A., Trac H., Cen R., Loeb A., 2013, ApJ, 776, 83
Bregmann J. N., 2007, ARA&A, 45, 221
Bull P., Clifton T., Ferreira P. G., 2012, Phys. Rev. D, 85, 4002
Castro P. G., 2004, Phys. Rev. D, 67, 044039; erratum-ibid., 2004, Phys. Rev. D, 70, 049902
Castro P. G., Heavens A. F., Kitching T. D., 2005, Phys. Rev. D, 72, 023516
Cen R., Ostriker J. P., 1999, ApJ, 514, 1
Cen R., Ostriker J. P., 2006, ApJ, 650, 560
Chang T.-C., Pen U.-L., Peterson J. B., McDonal P., 2008, Phys. Rev. Lett., 100, 091303
Cucchiara A. et al., 2011, ApJ, 736, 7
Dave R. et al., 2001, ApJ, 552, 473
DeDeo S., Spergel D. N., Trac H., 2005, preprint (arXiv:astro-ph/0511060)
Dodelson S., Jubas J. M., 1993, ApJ, 439, 503
Doré O., Hennawi J. F., Spergel D. N., 2004, ApJ, 606, 46
Edmonds A. R., 1996, Angular Momentum in Quantum Mechanics. Princeton Univ. Press, Princeton, NJ
February S., Clarkson C., Maartens R., 2013, J. Cosmol. Astropart. Phys., 1303, 023
Fukugita M., Peebles P. J. E., 2004, ApJ, 616, 643
Fukugita M., Peebles P. J. E., 2006, ApJ, 639, 590
Génova-Santos R., Atrio-Berandela F., Mucket J. P., Klar J. S., 2009, ApJ, 700, 447
George E. M. et al., 2015, ApJ, 799, 177
Grassi A., Schaefer B. J., 2014, MNRAS, 437, 2632
Gruzinov A., Hu W., 1998, ApJ 508, 435
Hall N. R. et al., 2010, ApJ, 718, 632
Hand N. et al., 2012, Phys. Rev. Lett., 109, 041101
Harker G. et al., 2010, MNRAS, 405, 2492
Heavens A., 2003, MNRAS, 343, 1327
Heavens A., Taylor A., 1995, MNRAS, 343, 1327
Heavens A. F., Kitching T. D., Taylor A. N., 2006, MNRAS, 373, 105
Hernández-Montegudo C., Trac H., Verde L., Jimenez R., 2006, ApJ, 652, L1
Hivon E., Gorski K. M., Netterfield C. B., Crill B. P., Prunet S., Hansen F., 2002, ApJ, 567, 2
Ho S., Dedeo S., Spergel D., 2009, preprint (arXiv:0903.2845)

Hu W., 2000, ApJ. 529, 12
Iliev I. T., Pen U.-L., Bond J. R., Mellema G., Shapiro P. R., 2007, ApJ, 660, 933
Jaffe A. H., Kamionkowski M., 1998, Phys. Rev. D, 58, 043001
Kashikawa N. et al., 2011, ApJ, 734, 119
Kashlinsky A., Atrio-Barandela F., Ebeling H., 2011, ApJ, 732, 1
Kashlinsky A., Atrio-Barandela F., Kocevski D., Ebeling H., 2008, ApJ, 686, L49
Kashlinsky A., Atrio-Barandela F., Ebeling H., Edge A., Kocevski D., 2010, ApJ, 712, L81
Kitching T. D., Heavens A. F., Miller L., 2011, MNRAS, 413, 2923
Kitching T. D. et al., 2014, MNRAS, 442, 1326
Kitching T. D., Heavens A. F., Das S., 2015, MNRAS, 449, 2205
Knox L., Scoccimarro R., Dodelson S., 1998, Phys. Rev. Lett., 81, 2004
Lonsdale C. J. et al., 2009, Proc. IEEE, 97, 1497
LoVerde M., Afshordi N., 2008, Phys. Rev. D, 78, 123506
Ma C.-P., Fry J. N., 2000, ApJ. 531, L87
Ma C.-P., Fry J. N., 2002, PRL, 88, 211301
Ma Y.-Z., Waerbeke L. V., Hinshaw G., Hojjati A., Scott D., 2014, preprint (arXiv:1404.4808)
McQuinn M., Furlanetto S. R., Hernquist L., Zahn O., Zaldarriga M., 2005, ApJ, 630, 657
Mesinger A., McQuinn M., Spergel D. N., 2012, 22, 1403
Mody K., Hajian A., 2012, ApJ, 758, 4
Morkczkowski T., Dicker S., Sayers E. D. et al., 2012, ApJ, 761, 47
Mortlock D. J. et al., 2011, Nat, 474, 616
Munshi D., Heavens A., Coles P., 2011, MNRAS, 411, 2161
Munshi D., Heavens A., Cooray A., Valageas P., 2011a, MNRAS, 414, 3173
Munshi D., Kitching T., Heavens A., Coles P., 2011b, MNRAS, 416, 629
Munshi D., Pratten G., Valageas P., Coles P., Brax P., 2015, preprint (arXiv:1508.00583)
Ostriker J. P., Vishniac E. T., 1986, ApJ, 306, L51
Ouchi M. et al., 2010, ApJ, 723, 869
Paciga G. et al., 2011, MNRAS, 413, 1174
Park H., Shapiro P. R., Komatsu E., Iliev I. T., Ahn K., Mellema G., 2013, ApJ, 769, 93
Park H., Komatsu E., Shapiro P. R., Koda J., Mao Y., 2016, ApJ, 818, 37
Parsons A. R. et al., 2010, AJ, 139, 1468
Peacock J. A., Dodds S. J., 1996, MNRAS, 280, 19
Penrose R., Rindler W., 1984, 1986, Spinors and Space-time Vol. 1 and 2. Cambridge Univ. Press, Cambridge
Planck Collaboration XXXVII, 2016, A&A, 586, 140
Pratten G., Munshi D., 2012, MNRAS, 423, 3209
Pratten G., Munshi D., 2013, MNRAS, 436, 3792
Pratten G., Munshi D., 2014, MNRAS, 442, 759
Rassat A., Refregier A., 2012, A&A, 540, A115
Riquelme M. A., Spergel D. N., 2007, ApJ, 661, 672R
Santos M. G., Cooray A., Haiman Z., Knox L., Ma C -P., 2003, ApJ, 630, 756
Shao J., Zhang P., Weipeng L., Jing Y., Pan J., 2011a, MNRAS, 413, 628
Shao J., Zhang P., Weipeng L., Jing Y., 2011b, ApJ, 730, 127
Shaw L. D., Rudd D. H., Nagai D., 2012, ApJ, 756, 15
Sunyaev R. A., Zeldovich Y. B., 1972, Comments on Astrophysics and Space Physics, Vol. 4. Gordon and Breach, New York, 173
Sunyaev R. A., Zeldovich Y. B., 1980, MNRAS, 190, 413
Valageas P., Balbi A., Silk J., 2001, A&A, 367, 1
Varshalovich D. A., Moskalev A. N., Khersonskii V. K., 1988, Quantum Theory of Angular Momentum. World Scientific Press, Singapore
Vishniac E. T., 1987, ApJ, 322, 597
White M., Song Y.-S., Percival W. J., 2009, MNRAS, 397, 1348
Xu X-D., Wang B., Zhang P., Atrio-Barandela F., 2013, J. Cosmol. Astropart. Phys., 12, 001
Yoo J., Desjacques V., 2013, Phys. Rev., 88, 023502
Zahn O., Mesinger A., McQuinn M., Tac H., Cen H., Cen R., Hernquist L. E., 2011, MNRAS, 414, 727
Zappacosta L., Nicastro F., Maiolino R., Tagliaferri G., Buote D. A., Fang T., Humphrey P. J., Gastaldello F., 2010, ApJ, 717, 74
Zhang P., 2010, MNRAS, 407, L36
Zhang P., Pen U.-L., 2001, ApJ, 549, 18
Zhang P., Pen U.-L., Trac H., 2004, MNRAS, 347, 1224

APPENDIX: RECONSTRUCTION IN A PARTIAL SKY

The power spectra we have constructed so far assume a full-sky coverage. In general surveys will not cover the entire sky. However, once survey configuration is specified by angular mask and selection function it is possible to use a pseudo-$\mathcal{C}_\ell$ (PCL) formalism in 3D to relate the observed $\mathcal{C}_\ell$s with the underlying 3D $\mathcal{C}_\ell$s. For the analytical derivation we will assume that the 3D mask $w_{3\rm D}(\boldsymbol{r})$ can be separated angular mask $w_{\rm a}(\hat{\boldsymbol{\Omega}})$ and the radial selection $w_{\rm r}(r)$ can be treated separately. Denoting the masked field by $\Theta^{\rm s\perp}(\boldsymbol{r})$ which is recovered from a survey and the underlying by $\Theta^{\perp}(\boldsymbol{r})$ we can write:

$$\Theta^{\rm s\perp}(\boldsymbol{r}) = w_{3\rm D}(\boldsymbol{r})\Theta^{\perp}(\boldsymbol{r}). \tag{A1}$$

We will assume a separable mask $w_{3\rm D}(\boldsymbol{r}) = w_{\rm r}(r)w_{\rm a}(\hat{\boldsymbol{\Omega}})$. This will allow us to deal with the angular and radial part separately making analytical treatment possible. The harmonic coefficients of the masked field and the underlying field are related by the following expression:

$$\Theta^{{\rm s}\perp}_{\ell m}(k) = \sum_{\ell' m'} \int dk'\ \Theta^{\perp}_{\ell' m'}(k') W^{\rm r}_{\ell\ell'}(k,k') \bar{W}^{\rm a}_{\ell m \ell' m'}. \tag{A2}$$

We will apply the same mask to the CMB $\Theta^{{\rm s}\perp}(\hat{\boldsymbol{\Omega}}) = w_{\rm a}(\hat{\boldsymbol{\Omega}})\Theta^{\perp}(\hat{\boldsymbol{\Omega}})$. The corresponding angular harmonics denoted respectively as $\Theta^{{\rm s}\perp}_{\ell m}$ and $\Theta^{\perp}_{\ell m}$ can be related as

$$\Theta^{{\rm s}\perp}_{\ell m} = \sum_{\ell' m'} \bar{W}^{\rm a}_{\ell m \ell' m'} \Theta^{\perp}_{\ell' m'}. \tag{A3}$$

The radial and angular mode-mixing matrices denoted as $W^{\rm r}$ and $\bar{W}^{\rm a}$ depends on the $w_{\rm r}$ and $w_{\rm a}$, respectively and can be expressed as follows:

$$W^{\rm r}_{\ell\ell'}(k,k') = \frac{2}{\pi} k\ k' \int dr\ r^2 w_r^2(r) j_\ell(kr) j_{\ell'}(k'r); \tag{A4}$$

$$\bar{W}^{\rm a}_{\ell\ell'} = \int d\hat{\boldsymbol{\Omega}}\ w(\hat{\boldsymbol{\Omega}})\ Y_{\ell m}(\hat{\boldsymbol{\Omega}})\ Y_{\ell' m'}(\hat{\boldsymbol{\Omega}}). \tag{A5}$$

The pseudo-$\mathcal{C}_\ell$s for the masked field $\Theta^{s\perp}(\mathbf{r})$ are denoted as $\mathcal{C}^{s\perp}_\ell(k)$ and $\mathcal{C}^{s\perp}_\ell(k_1,k_2)$. The pseudo $\mathcal{C}_\ell$s are linear combinations of the underlying $\mathcal{C}_\ell$s.

$$\mathcal{C}^{s\perp}_\ell(k) \equiv \left\langle \Theta^{s\perp}_{\ell m}(k) \Theta^{s\perp *}_{\ell m} \right\rangle = \sum_{\ell'} W^{\rm a}_{\ell\ell'} \int dk' W^{r}_{\ell\ell'}(k,k') \mathcal{C}^{\perp}_{\ell'}(k'); \tag{A6}$$

$$\mathcal{C}^{s\perp}_\ell(k_1,k_2) \equiv \left\langle \Theta^{s\perp}_{\ell m}(k) \Theta^{s\perp *}_{\ell m}(k) \right\rangle = \sum_{\ell'} W^{\rm a}_{\ell\ell'} \int dk'_1 \int dk'_2\ W^{\rm r}_{\ell\ell'}(k_1,k'_1)\ W^{\rm r}_{\ell\ell'}(k_2,k'_2) \mathcal{C}^{\perp}_{\ell'}(k'_1,k'_2). \tag{A7}$$

The linear transform relating the two power spectra e.g. $\mathcal{C}^{s\perp}_\ell(k)$ and $\mathcal{C}^{\perp}_\ell(k)$, or, equivalently $\mathcal{C}^{s\perp}_\ell(k_1,k_2)$ and $\mathcal{C}^{\perp}_\ell(k_1,k_2)$, are encapsulated in a mode-mixing matrix. However, due to our assumption of factorizability of the mask we can write the mixing matrix as product of two different mode-mixing matrices. The radial and angular mode-mixing matrices denoted as $W^{\rm r}$ and $W^{\rm a}$ depends on the $w_{\rm r}$ and $w_{\rm a}$, respectively and can be expressed as follows:

$$W^{\rm a}_{\ell\ell'} = \sum_L w_L \frac{I^2_{\ell L \ell'}}{2\ell+1} \begin{pmatrix} \ell & L & \ell' \\ 0 & 0 & 0 \end{pmatrix}^2; \qquad w_L = \frac{1}{2L+1} \sum_M w_{LM} w^*_{LM}. \tag{A8}$$

For nearly all-sky coverage the mixing matrices can be inverted to recover the underlying $\mathcal{C}_\ell$s. However, binning may be required for partial sky coverage. The power spectra $\mathcal{C}^{\parallel}_\ell(k)$ and $\mathcal{C}^{\parallel}_\ell(k,k')$ can be dealt with in an exactly similar manner. The mixing matrices remain unchanged.

It is possible to further simplify the expressions by using an approximate form for $j_\ell(x)$ valid at high ℓ (LoVerde & Afshordi 2008):

$$j_\ell(x)|_{\ell\to\infty} \approx \sqrt{\frac{\pi}{2\ell+1}} \delta_D \left(\ell + \frac{1}{2} - x \right). \tag{A9}$$

A few comments are in order. The PCL based sub-optimal estimators for projected or 2D data sets were developed by Hivon et al. (2002) in the context of CMB power-spectrum estimation. It has also been generalized for computation of cross-spectra involving external data sets (Munshi et al. 2011a). More recently, it has been extended for the 3D data by (Munshi et al. 2011b) and was successfully used for analysing 3D weak lensing power spectrum using CFHTLenS[19] data (Kitching et al. 2014). Though PCL based estimators remain sub-optimal, suitable use of weights can improve their performance.

The results presented here are generalization of the one presented in Munshi et al. (2011b) (where the effect of radial selection function was not included; i.e. $W^{\rm r} = 1$.) and will have general applicability in cross-correlating arbitrary projected field (3D) against a 3D cosmological tracer. Similar results can be derived for higher-order spin fields by suitably modifying $W^{\rm a}_{\ell\ell'}$.

Generalization to arbitrary spin. For the sake of completeness we also provide the expression for a generic 3D field with an *arbitrary* spin S α. We would like to cross-correlate it with another arbitrary projected field with spin S' say β. In this case the basis of expansion involves spinorial harmonics ${}_SY_{\ell m}(\hat{\boldsymbol{\Omega}})$. The spin-harmonics are defined in terms of D matrices as ${}_SY_{\ell m}(\hat{\boldsymbol{\Omega}}) \equiv \sqrt{\frac{2\ell+1}{4\pi}} D^{\ell}_{-S,m}(\theta,\phi,0)$ (Penrose & Rindler 1984, 1986; Varshalovich, Moskalev & Khersonskii 1988). The forward and backward transformations are obtained by replacing $Y_{\ell m}(\hat{\boldsymbol{\Omega}})$ in equations (11) and (12) with spin-weighted spherical harmonics or spinorial harmonics ${}_SY_{\ell m}(\hat{\boldsymbol{\Omega}})$:

$${}_S\alpha^s_{\ell m}(k) = \sum_{\ell' m'} \int dk'\ \alpha_{\ell' m'}(k') W^{\rm r}_{\ell\ell'}(k,k') {}_S\bar{W}^{\rm a}_{\ell m \ell' m'}; \tag{A10}$$

$${}_S\beta^s_{\ell m} = \sum_{\ell' m'} {}_S\bar{W}^{\rm a}_{\ell m \ell' m'} \beta_{\ell' m'}. \tag{A11}$$

[19] http://www.cfhtlens.org/

We follow the same notation as before but we assume the 3D field $\alpha(\boldsymbol{r})$ is a spinorial field of spin-weight S and $\beta(\hat{\boldsymbol{\Omega}})$ is a projected filed of spin S'. The harmonic components of these fields are now denoted as ${}_S\alpha_{\ell m}$ and ${}_{S'}\beta_{\ell m}$. The suffix s denotes quantities defined in partial sky. The radial component of the mixing matrix given in equation (A4) remains unchanged. However, the angular mode-mixing matrix depends on the spin of the specific field equation (A5).

$$ {}_S\bar{W}^{\rm a}_{\ell\ell'} = \int d\hat{\boldsymbol{\Omega}}\; w(\hat{\boldsymbol{\Omega}})\; {}_SY_{\ell m}(\hat{\boldsymbol{\Omega}})\; {}_SY^*_{\ell' m'}(\hat{\boldsymbol{\Omega}}). \tag{A12} $$

The corresponding auto- and cross-spectrum are defined as follows:

$$ \mathcal{C}^s_\ell(k) \equiv \left\langle \alpha^s_{\ell m}(k)\beta^{s*}_{\ell m}\right\rangle = \sum_{\ell'} {}_{SS'}W^{\rm a}_{\ell\ell'} \int dk' W^{\rm r}_{\ell\ell'}(k,k')\mathcal{C}_{\ell'}(k'); \tag{A13} $$

$$ \mathcal{C}^s_\ell(k_1,k_2) \equiv \langle \alpha_{\ell m}(k)\alpha^*_{\ell m}(k)\rangle = \sum_{\ell'} {}_{SS'}W^{\rm a}_{\ell\ell'} \int dk'_1 \int dk'_2\; W^{\rm r}_{\ell\ell'}(k_1,k'_1)\; W^{\rm r}_{\ell\ell'}(k_2,k'_2)\mathcal{C}_{\ell'}(k'_1,k'_2). \tag{A14} $$

These expressions generalizes the ones obtained in equations (A6) and (A7). The coupling matrix is denoted by ${}_{SS'}W^{\rm a}_{\ell\ell'}$ which is a generalization of the coupling matrix given in equation (A8):

$$ {}_{SS'}W^{\rm a}_{\ell\ell'} = \sum_L w_L \frac{I^2_{\ell L\ell'}}{2\ell+1} \begin{pmatrix} \ell & L & \ell' \\ S & 0 & -S \end{pmatrix} \begin{pmatrix} \ell & L & \ell' \\ S' & 0 & -S' \end{pmatrix}; \qquad w_L = \frac{1}{2L+1}\sum_M w_{LM}w^*_{LM}. \tag{A15} $$

Previous results correspond to the specific case when we set $S = S' = 0$. One immediate practical use of the above expressions could be joint analysis of CMB lensing and 3D galaxy lensing (Kitching, Heavens & Das 2015).

This paper has been typeset from a TEX/LATEX file prepared by the author.